Wintertime Brine Discharge at the Surface of a Cold Polar Glacier and the Unexpected Absence of Associated Seismicity

Chris G Carr[1,1], Joshua D Carmichael[2,2], and Erin Christine Pettit[3,3]

[1]Los Alamos National Laboratory
[2]Los Alamos National Laboratory (DOE)
[3]Oregon State University

November 30, 2022

Abstract

A subglacial groundwater system beneath Taylor Glacier discharges hypersaline, iron-rich brine episodically at the glacier surface to create Blood Falls; however, the triggering mechanism for these brine release events is not yet understood. We document wintertime brine discharge using time-lapse photography to show that the mechanism does not require melt-induced hydrofracture. Further, we analyze local seismic data to test a hypothesis that fracturing generates elevated surface wave energy preceding and/or coinciding with brine release events. Our results show no discernible elevated Rayleigh wave activity prior to or during Blood Falls brine release. Instead, we find a pattern of seismic events dominated by a seasonal signal, with more Rayleigh events occurring in the summer than the winter from the Blood Falls source area. We calculate that the volumetric opening of cracks that would generate Rayleigh waves at our detection limits are of similar size to myriad cracks in glacier ice, lake ice, and frozen sediment in the terminus area. We therefore propose that any fracturing coincident with brine release activity likely consists of a series of smaller opening events that are masked by other seismicity in the local environment.

Posted on 30 Nov 2022 — CC-BY-NC-ND 4 — https://doi.org/10.1002/essoar.10507440/v2 — This a preprint and has not been peer reviewed. Data may be preliminary.

Check for updates

Accepted Article

Wintertime Brine Discharge at the Surface of a Cold Polar Glacier and the Unexpected Absence of Associated Seismicity

C. G. Carr[1,2], J. D. Carmichael[2], E. C. Pettit[3]

[1]University of Alaska Fairbanks , Fairbanks, AK, USA
[2]Los Alamos National Laboratory, Los Alamos, NM, USA
[3]Oregon State University, Corvallis, OR, USA

Key Points:

- Time-lapse photos capture wintertime Blood Falls brine release.
- Brine release occurs without evidence for enhanced Rayleigh wave seismicity near the release point.
- The Blood Falls crack may open as a series of small fracture events, masked by local seismicity.

Corresponding author: Chris Carr, cgcarr@lanl.gov

This article has been accepted for publication and undergone full peer review but has not been through the copyediting, typesetting, pagination and proofreading process, which may lead to differences between this version and the Version of Record. Please cite this article as doi: 10.1029/2021JF006325.

This article is protected by copyright. All rights reserved.

Accepted Article

Abstract

A subglacial groundwater system beneath Taylor Glacier, Antarctica, discharges hypersaline, iron-rich brine episodically at the glacier surface to create Blood Falls. However, the triggering mechanism for these brine release events is not yet understood. Identifying which fracture processes are observed seismically can help us better characterize the hydrological system at Taylor Glacier, and more generally, provide us with a broader understanding of englacial hydrologic activity in cold glaciers. We document wintertime brine discharge using time-lapse photography. Subfreezing air temperatures during the brine discharge indicate that surface melt-induced hydrofracture is an unlikely trigger for brine release. Further, we analyze local seismic data to test a hypothesis that fracturing generates elevated surface wave energy preceding and/or coinciding with brine release events. Our results show no discernible elevated Rayleigh wave activity prior to or during Blood Falls brine release. Instead, we find a pattern of seismic events dominated by a seasonal signal, with more Rayleigh events occurring in the summer than the winter from the Blood Falls source area. We calculate that the volumetric opening of cracks that would generate Rayleigh waves at our detection limits are of similar size to myriad cracks in glacier ice, lake ice, and frozen sediment in the terminus area. We therefore propose that any fracturing coincident with brine release activity likely consists of a series of smaller opening events that are masked by other seismicity in the local environment.

Plain Language Summary

Blood Falls is a reddish feature that forms at the terminus of Taylor Glacier in Antarctica when hypersaline, iron-rich brine flows from sediment under the glacier up through the ice to emerge from cracks at the surface. We used data from a time-lapse camera and nearby seismic sensors to document a brine release. Our images show a brine release event starting in May 2014 (austral winter), and fractures in the glacier surface observed following the event encouraged us to hypothesize that we would detect an increase in Rayleigh waves (a type of seismic wave that can be generated by surface crack opening). However, we do not observe an increase in Rayleigh wave activity prior to or during brine release. When we estimate the average size of the fractures that we detect, we find the size is similar to many types of cracks in the nearby environment (for instance, cracks in the lake ice). We conclude that any Rayleigh wave seismicity that occurred during the Blood Falls brine release must be from a series of crack openings smaller than our detection limit, and that other cracks opening in the nearby environment may mask any signal specific to the Blood Falls release.

1 Introduction

Episodic discharge of subglacially-sourced, iron-rich brine at the terminus of Taylor Glacier, Antarctica, forms the feature named Blood Falls (Figure 1). The brine discharges over weeks to months during releases that occur several times per decade, and can occur during any season. Brine deposits have primarily been observed at two subaerial locations: the Blood Falls site at the glacier surface and, less frequently, at a lateral site where brine icings have been observed in the ice-marginal stream bed at the northern terminus margin. Compilations of brine release activity and brine deposit observations include Black (1969), Carr (2021), Keys (1979), and Lawrence (2017). In this paper we focus on the Blood Falls site; therefore, phrases like 'brine discharge' and 'brine release event' refer to discharge at the Blood Falls site unless otherwise specified.

An unresolved question is what triggers the episodic brine release. Carmichael et al. (2012) hypothesize that meltwater-driven fracturing during the summer melt season could propagate deep enough into the glacier to trigger brine outflow. However, springtime observations of brine icing superimposed on lake ice (e.g., Black, 1969; Keys, 1979) indirectly

This article is protected by copyright. All rights reserved.

suggest that brine releases can occur during the wintertime in the absence of surface melt. This implies that meltwater-driven fracture cannot explain all brine release events. Cracks in the glacier surface are often observed following a brine release event; these cracks extend tens of meters from the terminus up-glacier and can be on the order of tens of centimeters wide (Figure S1). These cracks observed near Blood Falls suggest that seismic activity could be used to monitor brine release activity. Seismometers are particularly helpful instruments during periods when human observers are not present, or when polar night makes time-lapse photography difficult.

Here, we use time-lapse photography to document a brine release event that began in winter 2014 (Figure 1). Large surface cracks were visible when researchers arrived the following summer field season (2014–2015, Figure S1). Surface crack opening generates Rayleigh waves, a type of seismic surface wave, including in glacial settings (e.g., Carmichael et al., 2015; Deichmann et al., 2000; Mikesell et al., 2012; Neave & Savage, 1970). Therefore, we test the hypothesis that the opening of Blood Falls-related cracks at the glacier surface generates detectable Rayleigh waves with elevated seismicity (number of seismic events per unit of time) prior to and/or during the brine release activity observed in the time-lapse photos from the winter.

Accepted Article

This article is protected by copyright. All rights reserved.

Figure 1. Time-lapse photos documenting a winter 2014 brine release event that was first visible on 13 May 2014. (a) Late summer photo prior to brine release, (b) winter photo of icing deposit after 17 days of brine discharge, (c)–(f) subsequent modification of the icing fan via melt, ablation, incision by liquids (surface meltwater and/or additional subglacially-sourced brine), and (g)–(h) further modification via flooding by the lateral stream and Lake Bonney moat.

Accepted Article

This article is protected by copyright. All rights reserved.

2 Background

2.1 Blood Falls: an Episodically Active Hydrologic Feature at Taylor Glacier

Taylor Glacier is an outlet glacier of the East Antarctic Ice Sheet. The glacier flows into Taylor Valley, where the central portion of the terminus ends in ice-capped Lake Bonney (Figure 2a). Typical ice temperatures are near -17°C in the terminus region (Pettit et al., 2014). The supraglacial component of the hydrologic system is active during the short melt season, typically from late November through mid January. During this time, most meltwater generated on the glacier either runs off the glacier in large supraglacial melt channels (Johnston et al., 2005) or pools in cryoconite holes (shallow ponds) that refreeze at the glacier surface (Fountain et al., 2004). Pathways for meltwater delivery into the glacier consist of crevasses, which are only present near the ice cliff margins and within the last few hundred meters of the terminus; moulins or similar deep connections to the englacial or subglacial components are absent.

Wintertime discharge events at Blood Falls result in the buildup of a fan-shaped icing deposit that drapes over the proglacial moraine and Lake Bonney ice surface (Black et al., 1965). Icings (also called naled, aufeis, or overflow) form in a variety of environmental settings when sub-surface water emerges and refreezes at the ground surface and have been documented at polythermal and cold-based glaciers. At these other glaciers, englacially- or subglacially-stored meltwater emerges at the ice surface or out of proglacial sediments to produce icings (e.g., Hodgkins et al., 2004; Irvine-Fynn et al., 2011; Skidmore & Sharp, 1999). At Taylor Glacier, summertime discharge events also occur, but do not create the same icings because the brine freezing point is much lower than typical summertime air temperatures. For terms like 'summertime', we follow the season definitions of Obryk et al. (2020) wherein the month of October is spring, November–February are summer, March is autumn, and April–September are winter.

Airborne electromagnetic surveys of Taylor Valley reveal several connected groundwater systems (Foley et al., 2016; Mikucki et al., 2015), including the subglacial groundwater system beneath the Taylor terminus. Blood Falls can be considered a groundwater spring and Lake Bonney a terminal lake in this system, with an estimated 1.5 km^3 of brine-saturated sediments extending under the ice for at least 6 km up-glacier from the lake (Mikucki et al., 2015). Ice thickness gradients resulting from highly incised surface channels in the terminus area impose strong hydraulic potential gradients at the glacier bed that route some subglacial flow towards Blood Falls and some towards the central terminus (Badgeley et al., 2017) where subglacial brine discharges directly into proglacial Lake Bonney (Lawrence et al., 2020). Less frequently, brine also discharges through sediment at lateral sites near the glacier margin (Carr, 2021, Chapter 2).

Following the winter 2014 brine release described in this paper, englacially-stored brine was sampled in-situ during the following summer field season (Badgeley et al., 2017; Campen et al., 2019; Kowalski et al., 2016; Lyons et al., 2019). The brine can remain liquid despite the cold ice temperatures due to salinity-driven freezing point depression, and presumably also due to latent heat effects. Geochemistry of the brine outflow at Blood Falls further suggests the subglacial brine has been isolated from the atmosphere for an extended time (Mikucki et al., 2009); stratigraphic evidence from drill cores in Taylor Valley suggest possible isolation since the late Miocene-early Pliocene (Elston & Bressler, 1981). Microbial analysis of brine collected from englacial storage following the winter 2014 event also supports the idea that the subglacial brine reservoir is isolated from solar energy due to the extremely low abundance of phototropic genetic sequences (Campen et al., 2019). The geochemistry of the englacially-stored brine that was sampled in situ as well as of brine discharged at the glacier surface indicates that the brine solutes represent ancient seawater that has been heavily modified through cryoconcentration and

This article is protected by copyright. All rights reserved.

Accepted Article

subglacial weathering (englacial brine geochemistry described by Lyons et al. (2019); geochemistry of brine sampled at the surface described by Mikucki et al. (2009)).

2.2 Taylor Glacier Seismicity and Hypotheses for Brine Release Mechanisms

Seismicity at the Taylor Glacier terminus region is characterized by strong seasonal patterns. Temporally variable environmental microseismicity (seismic activity from events smaller than the threshold) is known to influence the minimum event size that short-term average to long-term average (STA/LTA) algorithms can detect (Carr et al., 2020). During the summertime, seismicity varies diurnally when surface melt is absent and seismic events are located on the glacier and lake ice (Carmichael et al., 2012). However, when surface melt occurs, the diurnal seismicity pattern is suppressed and the event size and location pattern change. Seismic activity during melt periods consists of repeating, larger events with volumetric opening source mechanisms and locations consistent with crack opening in the Blood Falls area (Carmichael et al., 2012). Therefore, meltwater-driven surface crevassing was proposed as a possible mechanism for triggering Blood Falls brine release if the surface crevasses were able to propagate deep enough (Carmichael et al., 2012).

The winter 2014 brine release we document here occurred in the absence of surface melt (see Figure 3d for temperature data from a nearby meteorological station); therefore, we do not attribute the triggering of the winter 2014 event to meltwater-driven crevassing. Nonetheless, large surface cracks were observed following the winter 2014 brine release (Figure S1). Similar cracks have historically been observed following brine release events at the Blood Falls site (Carr, 2021, Chapter 2). We therefore developed a Rayleigh wave activity detector to monitor the Blood Falls source region for surface waves we expect to be generated by surface crevassing (e.g., Mikesell et al., 2012).

3 Data and Methods

3.1 Time-lapse Photos and Timestamp Correction

We deployed a time-lapse camera on the north side of the terminus with a side view of Blood Falls (Figure 1; co-located with station KRIS in Figure 2a). Intervals between photos are 2 hours except when power failure resulted in missing images. During installation, the time zone corresponding to the internal clock settings on the time-lapse camera was not recorded; we recognized this oversight during data review. Our time zone correction procedure is described in the Supporting Information (Text S1). The time-lapse photo data are available for public access through the U.S. Antarctic Program Data Center (Pettit, 2019).

3.2 Seismic Data and Rayleigh Wave Detector

We deployed a 3-seismometer network (Figure 2a). The network consisted of Sercel L-22 sensors (3-channel, 2 Hz sensors) that sampled surface motion at 200 Hz; power was provided by solar panel and battery assemblies. One seismometer (JESS) was installed on the glacier near Blood Falls and two (CECE, KRIS) in the frozen sediment at the lateral terminus margins. Seismometers were installed in November 2013 and removed in January 2015. Power loss at land-based station KRIS resulted in a data gap from 29 June 2014 – 1 October 2014. The other stations (CECE and JESS) recorded for the duration with no significant data gaps. We also excluded portions of the data for each station based on visual review of spectrograms confirming poor data quality on one or more channels (sample spectrograms included in Figures S2, S3, and S4). We used the remaining data as input into our Rayleigh detector. The seismic data are available for public access through the IRIS Data Management Center (Pettit, 2013).

This article is protected by copyright. All rights reserved.

Accepted Article

Accepted Article

We use a seismic correlation detector that is based on identifying statistically significant elliptically polarized energy. Raleigh waves are characterized by deformation in the vertical and radial directions (along the radial path from source to receiver), whereas Love waves consist of deformation in the transverse and radial directions (Stein & Wysession, 2003, p. 87–89). Rayleigh-wave detection operates on the principle that the elliptical polarized energy of a Rayleigh wave can be transformed to linearly polarized energy via a phase-shift of the vertical channel, while at the same time this transformation converts linearly polarized body waves and Love waves into elliptical polarization that do not trigger the correlation detector. Our algorithm modifies an automated Rayleigh-wave correlation detector routine described by Chael (1997). The detection of Raleigh waves from an unknown source typically requires knowing the timing of an event and scanning through possible source directions (defined as the back azimuth from the sensor) to find peak correlation values between the Hilbert-transformed vertical and rotated radial channels to infer a source location (e.g., Carmichael, 2013; Chael, 1997; Köhler et al., 2019). In contrast, we assume a known source location (Blood Falls) and monitor the correlation values through time to describe Rayleigh-wave seismicity originating along back azimuths pointing from the sensors towards Blood Falls (red arrows in Figure 2a).

Seismic detectors that test correlation statistics for the presence of seismic waveform energy are more sensitive than those that test for the presence of incoherent waveform energy, like a standard STA/LTA detector (Carmichael & Nemzek, 2019). Therefore, our detector has, in principle, the capability to identify waveforms of lower energy that originate from Blood Falls release locations compared to the STA/LTA detectors applied in our previous studies (Carr et al., 2020).

Our Rayleigh-wave detection algorithm operates as follows (Supporting Information Text S2 contains further details). For each station, we pre-process the data with detrending and bandpass filtering (passband 2.5–35 Hz) operations. We then rotate horizontal channels into a radial/transverse reference frame (methods follow Incorporated Research Institutions for Seismology (IRIS), 2020) with respect to Blood Falls (Figure 2a). Next, we Hilbert transform (phase advance by $\pi/2$ radians) the vertical channel. We calculate correlation coefficients between the aligned radial and Hilbert-transformed vertical channels with a 0.75 s, tapered, sliding window. Next, we define statistically significant thresholds for detection based on best-fit probability density functions calculated for consecutive 30-minute blocks of data (Figure 2b–c). The large-sample normality assumption for the correlation statistic is justified elsewhere (Wiechecki-Vergara et al., 2001).

To test the sensitivity of our results to our choice of threshold value, we run the algorithm with two different constant false alarm rates. A constant false alarm rate (CFAR) is defined as the probability that the detection statistic exceeds the threshold in the absence of a Rayleigh seismic event. Rayleigh events are declared when the correlation value between the radial and Hilbert-transformed vertical channel exceeds the specified threshold for at least 0.31 seconds. In our detector, a Rayleigh event declaration also requires a minimum temporal separation from preceding or succeeding events (3.29 seconds); if the temporal separation is less than this, the 'events' are grouped together as a single event (see example in Figure 2d). For Rayleigh events with correlation values above the threshold, we store the event duration, maximum correlation value, and associated p-value (area under the right hand tail of the correlation distribution, with the lower integration limit defined by the detection correlation statistic). For each 30-minute block we store quantitative routine output including the parameters that shape the best-fit correlation density function, such as the mean, standard deviation, and thresholds that associate with the different CFAR conditions we implement. Examples of detected waveforms are included in Figure S5. We also calculated the dominant frequency (following methods from Douma & Snieder, 2006) and event duration of identified events as described in Supporting Information Text S3 and Figures S6–S8.

This article is protected by copyright. All rights reserved.

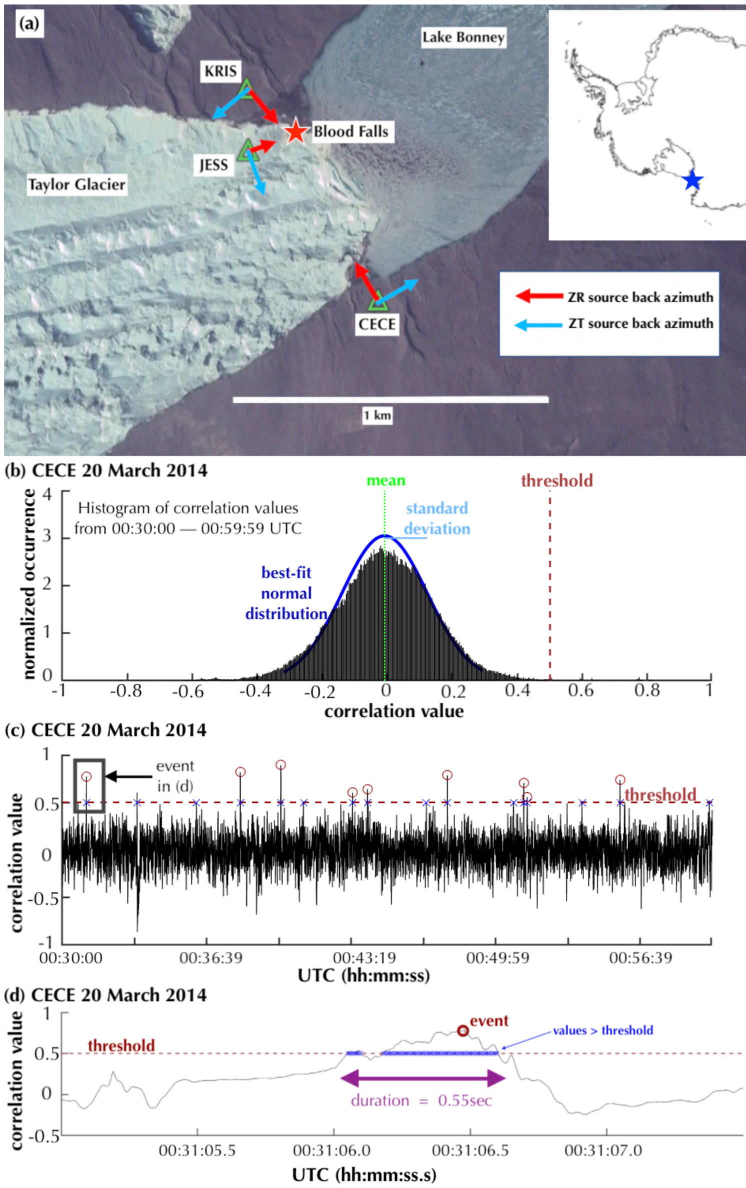

Figure 2. (a) Seismometer locations and back azimuth directions (arrows show direction, lengths are arbitrary). ZR detections indicate a Rayleigh wave traveling in the direction from Blood Falls to the seismometer. Base image: Google, Maxar Technologies, image date: 5 December 2008. (b) Theoretical density of the ZR correlation data (blue curve) and its histogram (bars) for a 30-minute window, normalized so the total area of the histogram bars equals one. The best-fit normal distribution has a mean of $-8.6\text{x}10^{-3}$ and standard deviation of 0.13. The one-sided CFAR condition of $5\text{x}10^{-5}$ dictates a threshold value of 0.50. (c) Correlogram and threshold corresponding to histogram in (b); 9 events (red circles) are identified above the threshold. Some correlation values exceeded the threshold (for instance: blue x's around minute 33); however, the short duration excludes these from being declared events. (d) Detail of the first event marked with box in (c). Blue x's: time indices with correlation values above the threshold. This is considered one event the gap between the two blocks of threshold exceedances is too short to distinguish separate events. The trigger on time is 00:31:06.045 (first blue x), trigger off time is 00:31:06.595 (last blue x), the red circle indicates the event time (00:31:06.465) and correlation value detection statistic (0.7742). The event duration is 0.55 seconds.

This article is protected by copyright. All rights reserved.

We ran the Rayleigh event detector with one-sided CFAR thresholds of 5x10^{-5} and 5x10^{-6} as a way to test the sensitivity of our results. We subjectively determined that these CFAR conditions provided the best compromise between smaller CFAR conditions wherein the detector skipped waveforms that we would have manually identified and larger CFAR conditions wherein the detector identified portions of seismograms that we could not visually attribute to Rayleigh-type signals rather than elliptically polarized background noise.

3.3 Rayleigh Detector Minimum Detectable Event Size Analysis

We perform an experiment to measure the temporal variability of the minimum event size identified by our Rayleigh detector. To do so, we estimate the minimum duration of a Rayleigh wave pulse excited by instantaneous crack formation, and then estimate both the high and low frequency limits of expected correlation between a radial and vertical channel after those waveforms are immersed in noise.

Our structural model uses physical parameters typical for cold glaciers (including seismic velocities and ice density) as well as experiment parameters specific to our 2013–2015 field seismic deployment (including the sampling interval and instrument response parameters). Specifically, we use p-wave and s-wave speeds of 3850 m/s and 1950 m/s for the ice layer and 4800 m/s and 2900 m/s for the substrate half-space (values from Carmichael et al., 2012; Shean et al., 2007). We use a standard ice density of 917 kg/m^3 and a substrate density of 2700 kg/m^3 consistent with basement velocities in Taylor Valley (Table 1, Barrett & Froggatt, 1978, and references therein). The crack for the template source event is a vertical crack at the glacier surface that opens with a volumetric change of 0.01 m^3, for instance, a crack with planar surface area of 1 m by 1 m that opens 0.01 m.

Our source model is a point source with a delta source time function that excites a Rayleigh wave. A sensor located 500 m from the seismic source records the Rayleigh waveform after this waveform attenuates in ice and thereby broadens, diminishes in amplitude, and superimposes with noise. We implement a Futterman filter (Futterman, 1962) to attenuate the waveform amplitude with $Q{=}\sqrt{(35 * 45)}$, the geometric mean of values reported by Carmichael et al. (2015, p. 12). The Futterman filter we implement is a causal filter that uses dispersive attenuation and a physical value of Q to reproduce the effect of reducing waveform amplitude at particular frequencies (Carmichael et al., 2015, equation 1). This attenuation broadens the peak asymmetrically so that energy cannot arrive before the propagation time from the source wavelet to the receiver (Figure 5.13, Aki & Richards, 2009). The 'noise', into which we infuse the attenuated Rayleigh waveform, is a random sample of the pre-processed (detrended, filtered, rotated) multichannel data from a specific 30-minute window; this sample is cut to the same length as the synthetic source waveform.

After adding the source waveform to the noise waveform, we calculate the correlation coefficient between the radial and Hilbert-transformed vertical waveform channels. We compare this correlation value with the threshold previously determined by the Rayleigh event detector for the 30-minute window the noise sample came from. If the correlation value of the template source superimposed on the noise sample does not exceed the threshold, we scale the source (scale the synthetic Rayleigh waveform) until the resulting correlation value exceeds the threshold.

We track the minimum detectable event size corresponding to the scaling required for the correlation to exceed the threshold, and repeat the experiment using thresholds and data samples from different 30-minute time windows. We completed the analysis for 3 weeks during the winter (10–30 May 2014).

We used the same source model to confirm the minimum pulse width that a delta-function source would produce for experimental conditions representative of our 2013-2015 seis-

Accepted Article

This article is protected by copyright. All rights reserved.

mic installation. We used an attenuation value of 40, consistent with elsewhere in the paper. We concluded that given a 500 m source to sensor distance with a Nyquist frequency of 100 Hz, the signal from a delta-function source that attenuates and convolves with the L-22 instrument response will have a duration of 0.4 s. For the frequency band we used, this equates to about one full cycle at 2.5 Hz or about 14 full cycles at 35 Hz (see Supporting Information Text S4 and Figures S9-S15 for details).

4 Results

4.1 Wintertime Brine Outflow

During the 2014 austral winter, a time-lapse camera captured brine outflow activity as a series of pulsed events, first visible on 13 May (Figure 1, Movie S1). Brine release continued through 8 June, after which darkness made data interpretation difficult, but outflow likely occurred through 28 June when power failure interrupted data collection (Movie S2). We refer to 13 May – 8 June 2014 as the initial visible brine release period. One image was captured on 22 August, a few images were captured in mid-September, and by the end of September regular image capture restarted because solar power was available for the system to resume data collection. During the three weeks of initial visible brine release, air temperatures recorded at a nearby meteorological station (approximately 3 km up-glacier from Blood Falls, Doran & Fountain, 2019) did not exceed −4.1°C and averaged −20.7°C; we therefore do not expect that any surface melt occurred.

The single image captured in August (Figure 1c) shows the fan surface had already been modified, presumably by sublimation. Subsequent, but infrequent, image collection shows that parts of the icing deposit were removed over the next several weeks. However, during October and early November, liquid is visible flowing down the icing surface (Figure 1e–f). We suspect this is additional Blood Falls brine, but cannot exclude the possibility that this is meltwater from preexisting icing deposits flowing down the icing fan. Melt channels incise the fan in mid-December, and the fan is more heavily modified by melt and sublimation. By mid-January at the end of the photo record, the icing deposit is much smaller than in prior months, partly because the lateral stream and melt from the edges of Lake Bonney flood the Blood Falls fan (Figure 1h).

4.2 Rayleigh-wave Event Detections

We plot the time series of Blood Falls back azimuth event detection rates (per 30 minutes) for the duration of the seismic data record in Figure S16, and from 1 Mar - 31 Aug 2014 in Figure 3. The initial visible brine release period (13 May – 8 June 2014) is highlighted in red. Gaps in the time series plots represent missing data (e.g., power failure at KRIS during July–mid-October) or when one or more channels were compromised. The North channel at CECE was not recording properly until the seismometer was serviced in late January 2014 (Figure S2), and all three channels at JESS failed as the 2014–2015 melt season progressed (Figure S4), presumably due to flooding of the installation by meltwater.

The same relative patterns of seismicity are apparent for both CFAR values. As expected, greater numbers of events are identified under the larger CFAR condition of $5\text{x}10^{-5}$ than $5\text{x}10^{-6}$ (Figure 3). We detect Rayleigh events during all times of the year, with the highest event detection rates in November – January. For part of the summertime at some stations, Rayleigh wave emission rate remains elevated (never returns to zero) for days at a time (see station JESS January 2014, Figure S16e and station KRIS January 2015 Figure S16c). Typical event detection rates are on the order of 0–30 events per 30 minutes under the CFAR=$5\text{x}10^{-6}$ condition, but vary seasonally and by station (Figures 3 and S16).

This article is protected by copyright. All rights reserved.

JESS recorded the highest 30-minute event rates of the winter on 13 May 2014, at the start of the visible brine release period (tallest red peak is 18 events per 30 minutes in Figure 3c). Other wintertime peaks at this station are typically around 9–12 events per 30 minutes. From around 20-27 May 2014, during the initial visible brine release period, land-based stations CECE and KRIS (Figure 3a,b) recorded event rates around 2–8 events per 30 minutes, similar to the rest of the winter.

Accepted Article

This article is protected by copyright. All rights reserved.

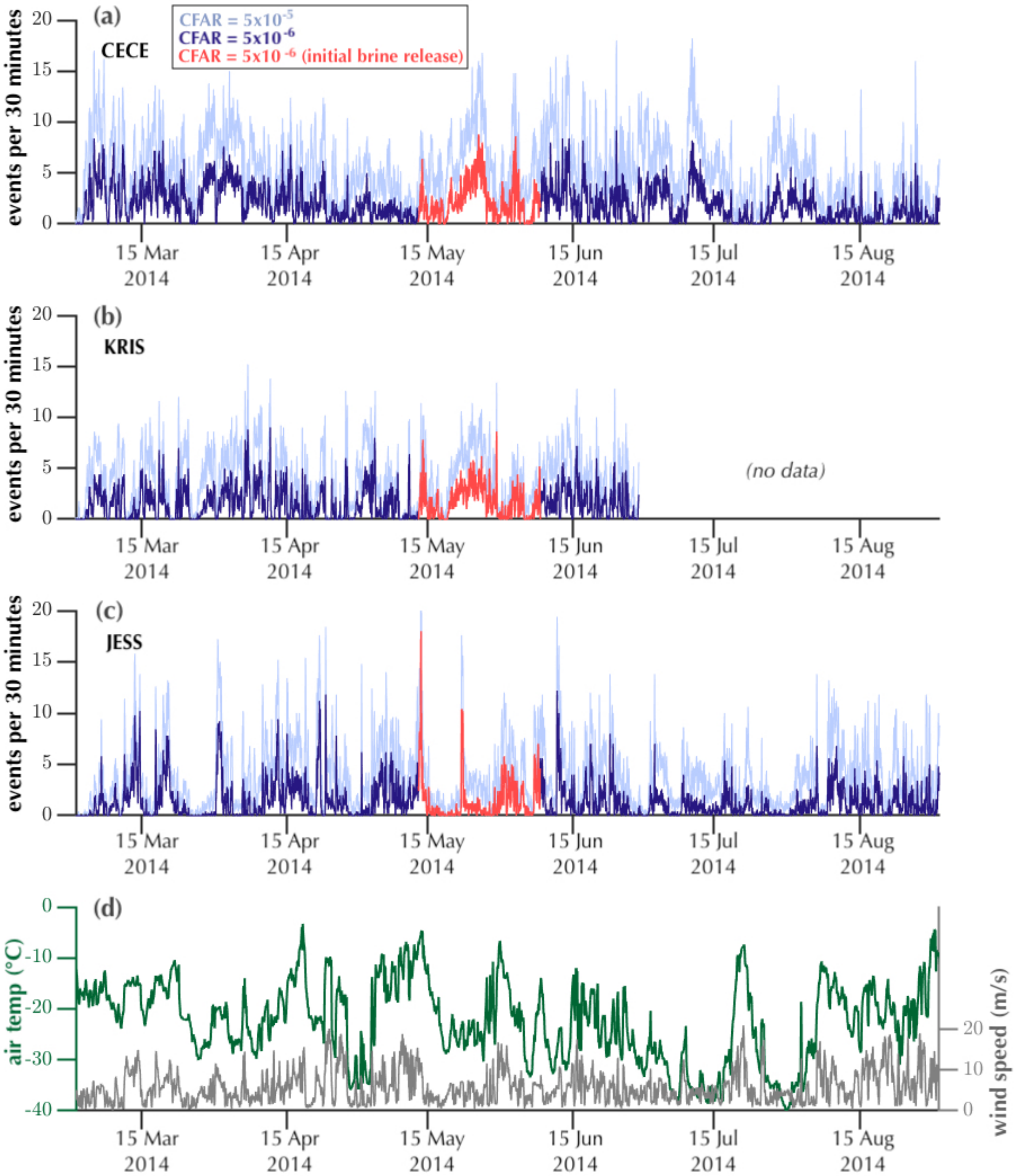

Figure 3. Events per 30 minutes, as identified by the Rayleigh-wave detector at (a) land-based station CECE, (b) land-based station KRIS (power failure caused data loss after June 30), and (c) on-ice station JESS (for this station, some rates above 20 events per 30 minutes identified using the 5x10^{-5} CFAR are cut off by the vertical scale, see Figure S16e for expanded scale). The CFAR = 5x10^{-6} condition is highlighted in dark blue and red (red indicates initial visible brine release period 13 May – 8 June 2014), and the 5x10^{-5} CFAR condition results are in light blue to show the range in detected event rates. In (d), air temperature (green, left vertical axis) and wind speed (grey, right vertical axis) from the nearby Taylor Glacier meteorological station (Doran & Fountain, 2019) are plotted. All time series are smoothed with a 2-hour duration (event detection rates: 5-point, weather data: 9-point) moving window. See Figure S16 in the supplemental information for time series covering the full data collection period.

This article is protected by copyright. All rights reserved.

Accepted Article

4.3 Detection Thresholds

We calculated the minimum event size detectable at each station for 30-minute windows from 10–30 May 2014. In Figure 4, crack size is reported in terms of crack edge length. We first calculated the minimum event size in terms of a volumetric opening (see Section 3.3), and converted this to the equivalent linear dimensions for a crack that opens 0.01 m and has a square planar area (crack depth = crack length, we define this as 'crack edge length'). Although we report our results in terms of edge length to facilitate comparison to cracks in the environment near Blood Falls, our results do not imply any specific crack aspect ratio or opening distance. The minimum detectable crack edge lengths average 2.2 m and 2.3 m, respectively, for land-based stations CECE and KRIS, and 2.9 m for on-ice station JESS for a crack opening 0.01 m. The pattern of smaller thresholds for the land-based stations during the wintertime compared to the on-ice station is consistent with prior results for this dataset where STA/LTA detectors were used to find events (Carr et al., 2020). For each station, there were 30-minute windows for which the minimum crack edge length that would be required to declare an event was larger than the maximum crack edge length that we tested (5.6 m), so the true minimum size is unknown. These windows are marked with red x's in Figure 4a-c.

Accepted Article

This article is protected by copyright. All rights reserved.

Accepted Article

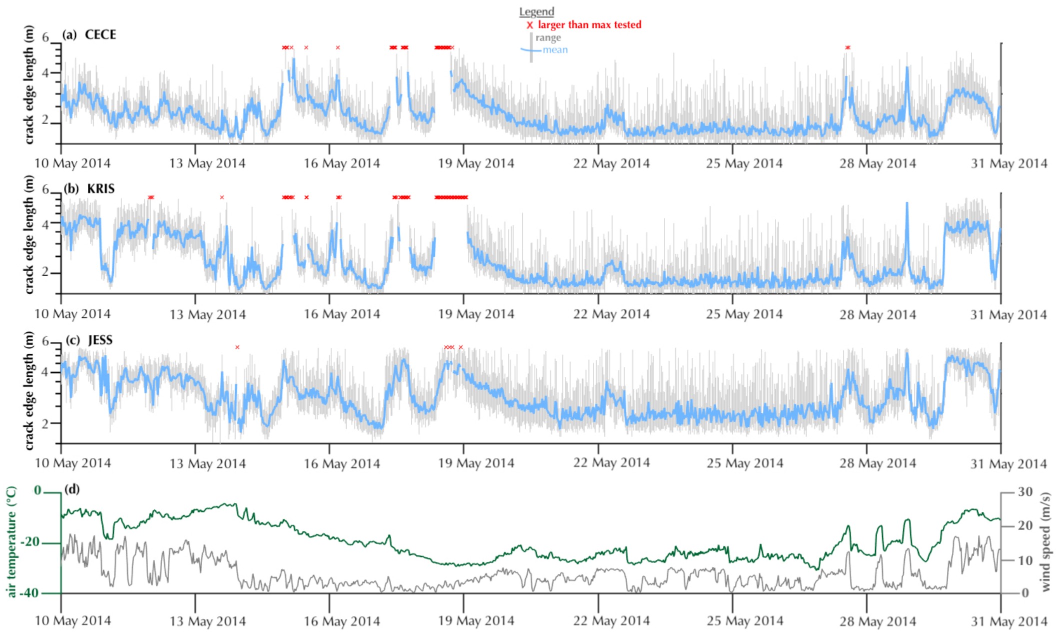

Figure 4. The smallest crack edge length (where crack edge length means the length of a side of a square planar crack that opens 0.01 m) for a Rayleigh wave-generating event that would trigger the detector at (a) CECE, (b) KRIS, and (c) JESS during 10–30 May 2014 under the 5x10^{-6} CFAR condition. We tested 15 different noise samples per 30-minute window. For each noise sample, we determined the minimum crack size required to generate correlation values larger than the CFAR-defined threshold. The bold blue line shows the mean of the minimum crack sizes for the 15 samples and the vertical grey bars show the range of minimum detectable crack sizes. Red x's indicate 30-minute windows for which the threshold crack edge length exceeds the maximum tested (5.6 m) for all noise samples (CECE: 38 windows, KRIS: 66 windows JESS: 5 windows, out of a total of 1008, 30-minute windows for each station). Note log scale of y-axis. (d) Air temperature (green, left vertical axis) and wind speed (grey, right vertical axis) measured at the Taylor meteorological station (Doran & Fountain, 2019). Some increases in mean minimum detectable crack edge length (particularly around 28 May 2014) appear to coincide with increases in wind speed and temperature, but the pattern is not simple.

This article is protected by copyright. All rights reserved.

5 Discussion

Meteorological data (Figure 3d) indicate that surface melt was not occurring during the wintertime brine outflow event. This suggests that this particular brine release was not triggered by a surface meltwater drainage event, as documented in other cold glacier settings (e.g., Boon & Sharp, 2003), and has been suggested as a potential triggering mechanism for Blood Falls brine release during the melt season (Carmichael et al., 2012). Further, our seismic analysis shows no distinct seismic signal associated with this brine release. We consider four possible reasons for the lack of observed seismic signature of brine release: 1) the seismic activity occurs outside of the frequency band we tested; 2) the seismic source is deeper than is detectable by our method; 3) the sources are smaller than our method can detect or aseismic; and 4) the sources are masked by myriad other environmental sources.

5.1 Hypotheses for the Apparent Lack of Brine Release Seismic Signatures

We do not observe an obvious increase in Rayleigh wave activity prior to or during brine release. A possible exception is the peak in event rate at JESS on 13 May 2014 (tallest red peak in Figure 3c), but the elevated event rate does not persist. The brief spike in event rate is not observed at the other stations. We also do not observe changes in event duration, event detection rates, or detection statistic values for Rayleigh events detected during the weeks prior to or during initial visible brine release. Instead, the dominant pattern of variation of Rayleigh-wave activity during our experiment is seasonal, with higher and more variable event detection rates during the summer. We also do not observe changes in dominant event frequency (Figure S6) or duration (Figure S8) relative to the rest of the wintertime.

5.1.1 Seismic Signature Outside the Frequency Bands of Our Experiment

The L-22 seismometers have a natural or corner frequency of 2 Hz, and for our installation the Nyquist frequency was 100 Hz (sample rate: 200 Hz). The Rayleigh detector used in this study as well as the STA/LTA detectors from our previous study (Carr et al., 2020) implement [2.5,35] Hz bandpass filters. This filter band is consistent with other Rayleigh-wave icequake studies (e.g., Carmichael et al., 2015; Hudson et al., 2020; Linder et al., 2019). Our Rayleigh detector imposed an effective minimum event duration of 0.31 seconds (see Supporting Information Text S2); we therefore cannot detect any events of shorter duration. The detector places no explicit constraint on maximum event duration (other than the theoretical limit of the 30-minute window length); the maximum event durations recorded are 30-40 seconds, though most events last less than 10 seconds (Figures S7 and S8). Nonetheless, the frequency and duration bands we sample are similar to previously reported Rayleigh wave seismicity associated with glacier surface crevassing. Köhler et al. (2019) found Rayleigh wave events consistent with modeled source depths of <10 m to have frequencies around 1-15 Hz, with durations of <1–6 seconds for sources 0.8–8 km away. With a bandpass filter of [10,80] Hz, Mikesell et al. (2012) found a dominant frequency of 45 Hz for Rayleigh wave events associated with surface crevasse opening for events located <600 m away. Carmichael (2013) similarly found Rayleigh wave events sourced by tensile surface fractures from a supraglacial lake drainage to show ~ 1 second durations and 25 Hz content. We therefore expect that if there are Rayleigh-wave generating surface crevassing events at our field site, our detector should find them based on our experimental design.

At higher frequency bands than that of our experiment, researchers have identified small seismic events located deep in glaciers. For instance, Helmstetter et al. (2015) observed repeating events characterized by short duration (0.1 s), high frequency (100 Hz), impul-

Accepted Article

This article is protected by copyright. All rights reserved.

Accepted Article

sive arrivals and distinct body waves but no surface waves, and determined that these events represented sources deep in the glacier. The event characteristics they describe agree with seismic events that other researchers have described as basal icequakes (e.g., Dalban Canassy et al., 2013; Deichmann et al., 2000; Walter et al., 2008). The short source duration of these sources implies small physical source dimensions; Helmstetter et al. (2015) attributed the seismic signals to stick-slip motion on the order of 1 μm to 4 mm of slip. We do not expect that our detector would identify such sources for several reasons, namely the lack of surface waves and the frequency characteristics and event duration outside our experimental design. If a similar mechanism at the bed (small-scale stick-slip motion) was responsible for perturbing the connection between the subglacial brine storage and potential englacial hydrologic pathways in such a way as to trigger Blood Falls brine release, we would not expect to detect such an initiation under our experimental conditions.

5.1.2 Deep Seismic Source

The source of brittle deformation associated with the brine release could be too deep in the glacier to generate surface waves that are large enough for us to observe. Rayleigh wave displacement decays with depth from the free surface. Therefore, the absence of observed elevated surface wave energy during Blood Falls brine release could indicate that any sources of seismic energy coinciding with brine release are located deeper in the glacier. To investigate this hypothesis, we estimate the source depths that would generate Rayleigh-wave energy at our detection threshold given our experimental design (see Supporting Information Text S5, Figure S17, and Table S1). We use the radiation pattern for a crack opening in the direction of the receiver to maximize the total displacement. We refer the reader to Carmichael (2021, equation 39) and Carr et al. (2020, Appendix C) for further documentation of the radiation pattern specific to the crack opening. We estimate that sources with depths around 2.5 km or deeper would evade detection because any Rayleigh displacement at the surface would be smaller than our detection limits. However, the glacier thickness near the terminus is much less than this estimated source depth; the glacier thickness near the terminus is tens of meters at the cliff edge, increasing to 125 m approximately 1 km up-glacier from the terminus (Badgeley et al., 2017; Pettit et al., 2014). We therefore expect that if basal crevasses excited Rayleigh wave energy, particularly in the shallow (<50 m) ice at the terminus, we would detect the events given our experimental design.

5.1.3 Events Smaller than Detection Thresholds

Another possibility is that seismicity associated with Blood Falls release is of such a small magnitude as to be effectively aseismic at our detection levels. The expected source scale for surface crack opening, based on field observations of the Blood Falls crack (e.g., Figure S1) is larger than our estimated detector thresholds for surface cracks that open and excite Rayleigh wave energy within our experiment's passband (Section 4.3). However, repeated cracking with volumetric opening smaller than the detection threshold of our detector could generate the cracks we see following a brine release event while evading detection. We cannot exclude this possibility.

Along the trend direction defined by projecting the Blood Falls crack system up-glacier, an englacial zone where liquid brine partially saturates the glacial ice causes reduced electromagnetic wave velocity, observable as a scattering zone in data collected through radio echo sounding (Badgeley et al., 2017). This documented zone of heterogeneity could also attenuate seismic waves. We did not include this possible attenuation in our source model for the minimum detectable event size analysis; if we were to, we expect the threshold crack edge length to be larger for sources within this zone of partially melted brine. As described in Section 3.3, we included a homogeneous attenuation value based on values reported by Carmichael et al. (2015).

This article is protected by copyright. All rights reserved.

5.1.4 Masked by Environmental Microseismicity

Another hypothesis is that there is a seismic signature associated with Blood Falls brine release, but it is superimposed on background emissions such that it is not statistically significant compared to the background (non-brine release) seismicity. The relative incoherence in measured seismic emission rates between sensors (Figure 3a–c) suggests that each receiver measures emission rates from Rayleigh wave sources that are a sum of Blood Falls and other background sources.

In the nearby environment (within a few meters to a few hundred meters of Blood Falls), there are many potential cryogenic crack sources, including cracking in the lake ice, surface cracking associated with ice cliff collapse near the terminus, and cracking of ice within the ice-cored moraines at the terminus (Figure S18). Our threshold detection analysis indicated that, at least for the three winter weeks we tested, the minimum crack sizes detectable at the land-based stations under the $5\text{x}10^{-6}$ CFAR condition have equivalent volumetric opening to cracks that are in the range of 2 m deep by 2 m long and opening 0.01 m. We know from our prior study (Carr et al., 2020) that environmental microseismicity influences STA/LTA-based event detection within this dataset, and consider it highly likely that it impacts Rayleigh-wave detection as well. Next, we consider possible environmental factors that we expect to contribute to Rayleigh-wave seismicity.

5.2 Wind, Meltwater, and Thermally-driven Environmental Microseismicity

Environmental factors may both contribute to Rayleigh wave activity and impact its detection. We expect the relative importance of factors like wind and meltwater to vary on seasonal timescales. For instance, meltwater-driven fracture consistent with seismicity reported by Carmichael et al. (2012) is likely responsible for some of the observed summertime Rayleigh-wave seismicity. Surface and subsurface melt in the uppermost tens of centimeters of the glacier are seasonally limited to the summertime (Hoffman et al., 2008), when air temperatures are near or above 0°C. Our record contains evidence of diurnal seismicity characteristics during the early summer months (November and December, Figure S16 in the Supporting Info), but as the summer progresses, the diurnal signal disappears (January, Figure S16). We also observed increased event rates in January that remain elevated for days (Figure S16). We agree with Carmichael et al. (2012) that the likely forcing factor is increased meltwater availability. The meltwater drives hydrofracture and reduces the observable seismic pattern of the early summer characterized by thermally-driven diurnal cycles.

The McMurdo Dry Valleys are characterized by different wind regimes in the summer than in the winter (Obryk et al., 2020); in the winter, foehn and less frequent katabatic wind events can dramatically raise local air temperatures by up to 30°C (Nylen et al., 2004; Speirs et al., 2010). Meteorological data from the Taylor Glacier station (Doran & Fountain, 2019) during the course of our experiment is consistent with the general climatology of the Dry Valleys. In the winter, wind speeds were higher, and the largest temperature changes occurred in association with strong wind events (Figure 3d). We infer that air-temperature changes associated with these wind events can cause fracture of various ice features as described below.

Temperature changes are known to cause ice fracture through several mechanisms. Thermally-induced crack formation can be sourced by thermal bending moments (MacAyeal et al., 2018), brittle fracture induced by thermal shock-sourced diffusion of heat at depth, and volumetric expansion of refreezing water at depth (Kovacs, 1992). Thermally-driven fracture also occurs in frozen sediment: Rayleigh waves have been observed in association with cracking of frozen sediment during rapid temperature drops (e.g., Okkonen et al., 2020).

This article is protected by copyright. All rights reserved.

Accepted Article

We suggest that year-round small seismic sources emanate from thermally-induced ice and frozen sediment fracture in the glacier terminus environment. Carmichael et al. (2012) located small seismic events on the lake ice consistent with thermal cracking. Field observations include thermally-induced cracking of the ice on Lake Bonney and ice-cored moraines (Figure S18) and ice blisters (Figure S19). Ice blisters can form after a confined water body develops an ice cover if continued freezing and expansion and/or hydrostatic pressure lift part of the ice cover upward into a dome shape (Kovacs, 1992). Ice blisters have been observed on supraglacial ponds on Taylor Glacier (CGC personal observation, Figure S19 and Text S6), brine icing deposits in the stream at the northern margin of Taylor Glacier (Keys, 1980, Plate 8.4) and in similar hydrologic settings in nearby Dry Valleys (Chinn, 1993, Figure 6). Because of the strong connection between wind events and temperature, we expect a direct impact on thermally-driven seismicity in association with wind events, although we did not explicitly test this hypothesis.

Despite the lack of conclusive seismic signature associated with brine release events, we can propose how brine release at Blood Falls may occur. Elevated brine pressure at the bed causes basal crevassing upwards into an englacial zone. If favorably oriented surface crevasses are present, brine flow can then reach the surface. We propose that the crack opening, both of basal crevasses and expansion of pre-existing surface crevasses, consists of a series of volumetrically small opening events that do not create a seismic signature sufficient to rise above the background microseismicity.

6 Conclusions

We document a wintertime brine release at Blood Falls that began in mid-May 2014 when air temperatures were well below freezing. We do not observe an increase in Rayleigh-wave activity prior to or during onset of the 2014 winter brine release, and therefore do not find evidence for surface meltwater-driven fracture as a mechanism for brine release. The lack of evidence for meltwater-driven fracture connecting the surface to the subglacial system is consistent with brine geochemistry that indicates the brine is isolated from the supraglacial meltwater system (Lyons et al., 2019; Mikucki et al., 2009).

In our Rayleigh wave event detection experiment, we did not find convincing evidence of a diagnostic seismic signature associated with the winter 2014 brine release at Blood Falls. We consider four hypotheses for the apparent lack of elevated Rayleigh-wave activity during brine release: 1) the seismic activity is outside our experimental frequency band; 2) the seismic activity is deep enough that surface waves are not recorded; 3) the crack opening is effectively aseismic (below our detection limits); and 4) environmental seismicity not related to brine release is sufficient to mask any seismicity associated with brine release.

As we review these hypotheses and in particular, the influence that environmental microseismicity plays both in generating seismic signals and masking detection of non-environmental seismic signals, we cannot exclude the case that surface and/or basal crevasses occur at sizes below our detection limits. An example of how environmental microseismicity modulates event detection is the temporal variation in the size of the smallest detectable crack opening. We find that the smallest events we can detect are comparable in size to myriad cracks in the nearby glacial terminus environment (including cracks in lake ice, ice-cored moraines, ice-lidded supraglacial ponds, and the glacier surface itself). The minimum detectable event size analysis is a robust tool that can be used to characterize detector sensitivity in other noisy seismic environments.

Acknowledgments
The U.S. National Science Foundation (NSF) Office of Polar Programs funded this work with a grant to E.C.P. (1144177). The PASSCAL Instrument Center (IRIS, NSF EAR-

This article is protected by copyright. All rights reserved.

Accepted Article

0552316, 1063471) provided seismic support. This work was conducted in cooperation with the Enceladus Explorer (EnEx) project (PI Bernd Dachwald) through grants 50NA1206 to 50NA1211 from the DLR Space Administration, and as a collaborative project with NSF grants to Jill Mikucki (1619795), Slawek Tulaczyk, (1144192), and Berry Lyons (1144176). We thank Jessica Badgeley, Doug Bloomquist, Paul Carpenter, Susan Detweiler, Jennifer Erxleben, Tiffany Green, Jason Herbert, Cecelia Mortenson, and Thomas Nylen for their field assistance during the 2013–2014 and 2014–2015 field seasons.

Time-lapse photo data are available through the U.S. Antarctic Program Data Center (Pettit, 2019) at `https://www.usap-dc.org/view/dataset/601167`. Seismic data (Pettit, 2013) are available through the International Federation of Digital Seismograph Networks via the IRIS Data Management Center at `https://www.fdsn.org/networks/detail/YW_2013`.

In addition to code written by C.G.C. and J.D.C., we thank Kate Allstadt and Ken Creager for code development. Carl Tape, Martin Truffer, and three anonymous reviewers provided valuable feedback on this manuscript.

This manuscript has been authored with number LA-UR-21-24023 by Triad National Security under Contract with the U.S. Department of Energy, Office of Defense Nuclear Nonproliferation Research and Development. The United States Government retains and the publisher, by accepting the article for publication, acknowledges that the United States Government retains a non-exclusive, paid-up, irrevocable, world-wide license to publish or reproduce the published form of this manuscript, or allow others to do so, for United States Government purposes.

References

Aki, K., & Richards, P. G. (2009). *Quantitative Seismology* (Second ed.). Mill Valley, CA, USA: University Science Books.

Badgeley, J. A., Pettit, E. C., Carr, C. G., Tulaczyk, S., Mikucki, J. A., Lyons, W. B., & MIDGE Science Team. (2017). An englacial hydrologic system of brine within a cold glacier: Blood Falls, McMurdo Dry Valleys, Antarctica. *Journal of Glaciology*, *63*(239), 387–400. doi: 10.1017/jog.2017.16

Barrett, P. J., & Froggatt, P. C. (1978). Densities, porosities, and seismic velocities of some rocks from Victoria Land, Antarctica. *New Zealand Journal of Geology and Geophysics*, *21*(2), 175–187. doi: 10.1080/00288306.1978.10424049

Black, R. F. (1969). Saline discharges from Taylor Glacier, Victoria Land, Antarctica. *Antarctic Journal of the United States*, *4*(3), 89–90.

Black, R. F., Jackson, M. L., & Berg, T. E. (1965). Saline discharge from Taylor Glacier, Victoria Land, Antarctica. *The Journal of Geology*, *73*(1), 175–181. doi: 10.1086/627053

Boon, S., & Sharp, M. (2003). The role of hydrologically-driven ice fracture in drainage system evolution on an Arctic glacier. *Geophysical Research Letters*, *30*(18), 4 pp. doi: 10.1029/2003GL018034

Campen, R., Kowalski, J., Lyons, W. B., Tulaczyk, S., Dachwald, B., Pettit, E., ... Mikucki, J. A. (2019). Microbial diversity of an Antarctic subglacial community and high-resolution replicate sampling inform hydrological connectivity in a polar desert. *Environmental Microbiology*, *21*(7), 2290–2306. doi: 10.1111/1462-2920.14607

Carmichael, J. D. (2013). *Melt-triggered seismic response in hydraulically-active polar ice: Observations and methods* (Doctoral dissertation, University of Washington, Seattle, Seattle, WA, USA). Retrieved from `http://hdl.handle.net/1773/25007`

Carmichael, J. D. (2021). Hypothesis tests on Rayleigh wave radiation pattern shapes: a theoretical assessment of idealized source screening. *Geophysical*

This article is protected by copyright. All rights reserved.

Accepted Article

Journal International, *225*(3), 16531671. doi: 10.1093/gji/ggab055
Carmichael, J. D., Joughin, I., Behn, M. D., Das, S., King, M. A., Stevens, L., & Lizarralde, D. (2015). Seismicity on the western Greenland Ice Sheet: Surface fracture in the vicinity of active moulins. *Journal of Geophysical Research F: Earth Surface*, *120*(6), 1082–1106. doi: 10.1002/2014JF003398
Carmichael, J. D., & Nemzek, R. J. (2019). Uncertainty in the predictive capability of detectors that process waveforms from explosions. *arXiv preprint*, 40 pp. Retrieved from http://arxiv.org/abs/1906.09350
Carmichael, J. D., Pettit, E. C., Hoffman, M., Fountain, A., & Hallet, B. (2012). Seismic multiplet response triggered by melt at Blood Falls, Taylor Glacier, Antarctica. *Journal of Geophysical Research: Earth Surface*, *117*(F3), 16 pp. doi: 10.1029/2011JF002221
Carr, C. G. (2021). *Blood Falls, Taylor Glacier, Antarctica: Subglacially-Sourced Outflow at the Surface of a Cold Polar Glacier as Recorded by Time-Lapse Photography, Seismic Data, and Historical Observations* (Doctoral dissertation, University of Alaska Fairbanks, Fairbanks, AK, USA). Retrieved from https://www.proquest.com/docview/2504856734
Carr, C. G., Carmichael, J. D., Pettit, E. C., & Truffer, M. (2020). The influence of environmental microseismicity on detection and interpretation of small-magnitude events in a polar glacier setting. *Journal of Glaciology*, *66*(259), 790–806. doi: 10.1017/jog.2020.48
Chael, E. P. (1997). An automated Rayleigh-wave detection algorithm. *Bulletin of the Seismological Society of America*, *87*(1), 157–163.
Chinn, T. J. (1993). Physical hydrology of the Dry Valley lakes. In W. J. Green & E. I. Friedmann (Eds.), *Physical and Biogeographical Processes in Antarctic Lakes* (Vol. 59, pp. 1–51). Washington, D.C., USA: American Geophysical Union. doi: 10.1029/AR059p0001
Dalban Canassy, P., Walter, F., Husen, S., Maurer, H., Faillettaz, J., & Farinotti, D. (2013). Investigating the dynamics of an alpine glacier using probabilistic icequake locations: Triftgletscher, Switzerland. *Journal of Geophysical Research: Earth Surface*, *118*(4), 2003–2018. doi: 10.1002/jgrf.20097
Deichmann, N., Ansorge, J., Scherbaum, F., Aschwanden, A., Bernardi, F., & Gudmundsson, G. H. (2000). Evidence for deep icequakes in an Alpine glacier. *Annals of Glaciology*, *31*, 85–90. doi: 10.3189/172756400781820462
Doran, P. T., & Fountain, A. G. (2019). *McMurdo Dry Valleys LTER: High frequency measurements from Taylor Glacier Meteorological Station (TARM) in Taylor Valley, Antarctica from 1994 to present.* Environmental Data Initiative. doi: 10.6073/pasta/a1df5cdab3319e9adeb18f8448fd363e
Douma, H., & Snieder, R. (2006). Correcting for bias due to noise in coda wave interferometry. *Geophysical Journal International*, *164*(1), 99–108. doi: 10.1111/j.1365-246X.2005.02807.x
Elston, D. P., & Bressler, S. L. (1981). Magnetic stratigraphy of DVDP drill cores and late Cenozoic history of Taylor Valley, Transantarctic Mountains, Antarctica. In L. D. McGinnis (Ed.), *Dry Valley Drilling Project* (Vol. 33, pp. 413–426). Washington, D.C., USA: American Geophysical Union. doi: 10.1029/AR033p0413
Foley, N., Tulaczyk, S., Auken, E., Schamper, C., Dugan, H., Mikucki, J., ... Doran, P. (2016). Helicopter-borne transient electromagnetics in high-latitude environments: an application in the McMurdo Dry Valleys, Antarctica. *Geophysics*, *81*(1), WA87–WA99. doi: 10.1190/geo2015-0186.1
Fountain, A. G., Tranter, M., Nylen, T. H., Lewis, K. J., & Mueller, D. R. (2004). Evolution of cryoconite holes and their contribution to meltwater runoff from glaciers in the McMurdo Dry Valleys, Antarctica. *Journal of Glaciology*, *50*(168), 35–45. doi: 10.3189/172756504781830312
Futterman, W. I. (1962). Dispersive body waves. *Journal of Geophysical Research*,

Accepted Article

This article is protected by copyright. All rights reserved.

67(13), 5279-5291. doi: 10.1029/JZ067i013p05279

Helmstetter, A., Nicolas, B., Comon, P., & Gay, M. (2015). Basal icequakes recorded beneath an Alpine glacier (Glacier d'Argentière, Mont Blanc, France): Evidence for stick-slip motion? *Journal of Geophysical Research: Earth Surface*, *120*(3), 379–401. doi: 10.1002/2014JF003288

Hodgkins, R., Tranter, M., & Dowdeswell, J. A. (2004). The characteristics and formation of a High-Arctic proglacial icing. *Geografiska Annaler Series A: Physical Geography*, *86*(3), 265–275. doi: 10.1111/j.0435-3676.2004.00230.x

Hoffman, M. J., Fountain, A. G., & Liston, G. E. (2008). Surface energy balance and melt thresholds over 11 years at Taylor Glacier, Antarctica. *Journal of Geophysical Research*, *113*(F4), 12 pp. doi: 10.1029/2008JF001029

Hudson, T. S., Brisborne, A., White, R., Kendall, J., Arthern, R., & Smith, A. (2020). Breaking the ice: identifying hydraulically forced crevassing. *Geophysical Research Letters*, *47*, 9 pp. doi: 10.1029/2020GL090597

Incorporated Research Institutions for Seismology (IRIS). (2020). *IRIS DMC IRISWS rotation Web Service Documentation.* http://service.iris.edu/irisws/rotation/1/.

Irvine-Fynn, T. D. L., Hodson, A. J., Moorman, B. J., Vatne, G., & Hubbard, A. L. (2011). Polythermal glacier hydrology: a review. *Reviews of Geophysics*, *49*(4), 37 pp. doi: 10.1029/2010RG000350

Johnston, R. R., Fountain, A. G., & Nylen, T. H. (2005). The origin of channels on lower Taylor Glacier, McMurdo Dry Valleys, Antarctica, and their implication for water runoff. *Annals of Glaciology*, *40*, 1–7. doi: 10.3189/172756405781813708

Keys, J. R. (1979). Saline discharge at the terminus of Taylor Glacier. *Antarctic Journal of the United States*, *14*(5), 82–85.

Keys, J. R. (1980). *Salts and their distribution in the McMurdo region, Antarctica* (Doctoral dissertation, Victoria University of Wellington, Wellington, New Zealand). Retrieved from `http://hdl.handle.net/10063/760`

Köhler, A., Maupin, V., Nuth, C., & van Pelt, W. (2019). Characterization of seasonal glacial seismicity from a single-station on-ice record at Holtedahlfonna, Svalbard. *Annals of Glaciology*, *60*(79), 23–36. doi: 10.1017/aog.2019.15

Kovacs, A. (1992). *Glacier, river and sea ice blister observations* (Tech. Rep.). Hanover, NH, USA: U.S. Army Corps of Engineers, Cold Regions Research and Engineering Laboratory.

Kowalski, J., Linder, P., Zierke, S., von Wulfen, B., Clemens, J., Konstantinidis, K., ... Helbing, K. (2016). Navigation technology for exploration of glacier ice with maneuverable melting probes. *Cold Regions Science and Technology*, *123*, 53–70. doi: 10.1016/j.coldregions.2015.11.006

Lawrence, J. P. (2017). *Evidence of subglacial brine inflow and wind-induced seiching from high temporal resolution temperature measurements in Lake Bonney, Antarctica* (Master's Thesis, Louisiana State University, Baton Rouge, LA, USA). Retrieved from `https://digitalcommons.lsu.edu/gradschool_theses/4343`

Lawrence, J. P., Doran, P. T., Winslow, L. A., & Priscu, J. C. (2020). Subglacial brine flow and wind-induced internal waves in Lake Bonney, Antarctica. *Antarctic Science*, *32*(3), 223–237. doi: 10.1017/s0954102020000036

Linder, F., Laske, G., Water, F., & Doran, A. K. (2019). Crevasse-induced Rayleigh-wave azimuthal anisotropy on Glaceir de la Paine Morte, Switzerland. *Annals of Glaciology*, *60*(79), 96–111. doi: 10.1017/aog.2018.25

Lyons, W. B., Mikucki, J. A., German, L. A., Welch, K. A., Welch, S. A., Gardner, C. B., ... Dachwald, B. (2019). The geochemistry of englacial brine from Taylor Glacier, Antarctica. *Journal of Geophysical Research: Biogeosciences*, *124*(3), 633–648. doi: 10.1029/2018JG004411

MacAyeal, D. R., Banwell, A. F., Okal, E. A., Lin, J., Willis, I. C., Goodsell, B.,

This article is protected by copyright. All rights reserved.

Accepted Article

Accepted Article

& MacDonald, G. J. (2018). Diurnal seismicity cycle linked to subsurface melting on an ice shelf. *Annals of Glaciology*, *60*(79), 137–157. doi: 10.1017/aog.2018.29

Mikesell, T. D., van Wijk, K., Haney, M. M., Bradford, J. H., Marshall, H. P., & Harper, J. T. (2012). Monitoring glacier surface seismicity in time and space using Rayleigh waves. *Journal of Geophysical Research*, *117*(F2), 12 pp. doi: 10.1029/2011JF002259

Mikucki, J. A., Auken, E., Tulaczyk, S., Virginia, R. A., Schamper, C., Sørensen, K. I., . . . Foley, N. (2015). Deep groundwater and potential subsurface habitats beneath an Antarctic dry valley. *Nature Communications*, *6*(6831), 9 pp. doi: 10.1038/ncomms7831

Mikucki, J. A., Pearson, A., Johnston, D. T., Turchyn, A. V., Farquhar, J., Schrag, D. P., . . . Lee, P. A. (2009). A contemporary microbially maintained subglacial ferrous "ocean". *Science*, *324*(5925), 397–400. doi: 10.1126/science.1167350

Neave, K. G., & Savage, J. C. (1970). Icequakes on the Athabasca Glacier. *Journal of Geophysical Research*, *75*(8), 1351–1362. doi: 10.1029/JB075i008p01351

Nylen, T. H., Fountain, A. G., & Doran, P. T. (2004). Climatology of katabatic winds in the McMurdo Dry Valleys, southern Victoria Land, Antarctica. *Journal of Geophysical Research*, *109*(D03114), 9 pp. doi: 10.1029/2003JD003937

Obryk, M. K., Doran, P. T., Fountain, A. G., Myers, M., & McKay, C. P. (2020). Climate from the McMurdo Dry Valleys, Antarctica, 1986–2017: Surface air temperature trends and redefined summer season. *Journal of Geophysical Research: Atmospheres*, *125*(13), 14 pp. doi: 10.1029/2019JD032180

Okkonen, J., Neupauer, R. M., Kozlovskaya, E., Afonin, N., Moisio, K., Taewook, K., & Muurinen, E. (2020). Frost quakes: Crack formation by thermal stress. *Journal of Geophysical Research: Earth Surface*, *125*(9), 14 pp. doi: 10.1029/2020JF005616

Pettit, E. C. (2013). MIDGE: Minimally Invasive Direct Glacial Exploration of Biogeochemistry, Hydrology and Glaciology of Blood Falls, McMurdo Dry Va. International Federation of Digital Seismograph Networks. *International Federation of Digital Seismograph Networks*. doi: 10.7914/SN/YW_2013

Pettit, E. C. (2019). Time lapse imagery of the Blood Falls feature, Antarctica. *U.S. Antarctic Program (USAP) Data Center*. doi: 10.15784/601167

Pettit, E. C., Whorton, E. N., Waddington, E. D., & Sletten, R. S. (2014). Influence of debris-rich basal ice on flow of a polar glacier. *Journal of Glaciology*, *60*(223), 989–1006. doi: 10.3189/2014JoG13J161

Shean, D. E., Head III, J. W., & Marchant, D. R. (2007). Shallow seismic surveys and ice thickness estimates of the Mullins Valley debris-covered glacier, McMurdo Dry Valleys, Antarctica. *Antarctic Science*, *19*(4), 485–496. doi: 10.1017/S0954102007000624

Skidmore, M. L., & Sharp, M. J. (1999). Drainage system behaviour of a High-Arctic polythermal glacier. *Annals of Glaciology*, *28*, 209–215. doi: 10.3189/172756499781821922

Speirs, J. C., Steinhoff, D. F., McGowan, H. A., Bromwich, D. H., & Monaghan, A. J. (2010). Foehn winds in the McMurdo Dry Valleys, Antarctica: the origin of extreme warming events. *Journal of Climate*, *23*(13), 3577–3598. doi: 10.1175/2010JCLI3382.1

Stein, S., & Wysession, M. (2003). *An Introduction to Seismology, Earthquakes, and Earth Structure.* Malden, MA, USA: Blackwell Publishing.

Walter, F., Deichmann, N., & Funk, M. (2008). Basal icequakes during changing subglacial water pressures beneath Gornergletscher, Switzerland. *Journal of Glaciology*, *54*(186), 511–521. doi: 10.3189/002214308785837110

Wiechecki-Vergara, S., Gray, H. L., & Woodward, W. A. (2001). *Statistical Development in Support of CTBT Monitoring.* Dallas, TX, USA: Southern Methodist

This article is protected by copyright. All rights reserved.

818 University.

Accepted Article

This article is protected by copyright. All rights reserved.

Supporting Information for "Wintertime Brine Discharge at the Surface of a Cold Polar Glacier and the Unexpected Absence of Associated Seismicity"

C. G. Carr[1,2], J. D. Carmichael[2], E. C. Pettit[3]

[1]University of Alaska Fairbanks, Fairbanks, AK, USA

[2]Los Alamos National Laboratory, Los Alamos, NM, USA

[3]Oregon State University, Corvallis, OR, USA

Contents of this file

1. Text S1 to S6
2. Figures S1 to S19
3. Table S1

Additional Supporting Information (Files uploaded separately)

1. Captions for Movies S1 to S2

Introduction

This supporting information includes: descriptions of the time-lapse photo timestamp correction (Text S1), details of the Rayleigh wave detection method (Text S2), dominant frequency and event duration analysis (Text S3), minimum pulse and phase sensitivity

---

Corresponding author: Chris G. Carr, Los Alamos National Laboratory, Los Alamos, NM 87544, USA (cgcarr@lanl.gov)

analysis (Text S4), source depth analysis (Text S5), and context for the 19 additional figures, 1 table, and 2 movies (description and context in Text S6).

Text S1. Time-lapse Photo Timestamp Correction

Upon review of data collected by the time-lapse camera, we realized that the time zone corresponding to the internal camera clock had not been recorded. Field photos taken on personal cameras during the time-lapse camera installation as well as metadata from a co-located seismometer guided our time zone correction of the time-lapse images from the camera. The camera time appears to correspond to UTC-13 at the time of installation, and the camera clock observes daylight savings time following the dates for the United States. We therefore add 12 hours for timestamps between 9 March and 2 November 2014, and add 13 hours during the rest of the year. We estimate that our corrected times of day are within about 1–2 hours of the true time of day based on sunlight patterns. Despite the lack of temporal accuracy, we can still make observations about the relative timing of brine release pulses as well as erosional and depositional characteristics; however, we cannot tie any specific photo to discrete seismic events. We note that even with accurate timestamps, the relatively coarse time resolution of the photos (1 sample every 2 hours) would hinder direct correlation with specific events in the seismic record (200 samples per second).

Text S2. Rayleigh Wave Detection Method

Rayleigh waves are seismic waves characterized by out-of-phase displacement in the vertical and radial plane that connects the seismic source to the sensor; displacement decays exponentially with depth from the surface. Particle motion plots of the vertical component of surface motion against the horizontal component show retrograde (counter-clockwise), elliptical motion in the direction of wave propagation, as a function of time (Stein & Wysession, 2003, p. 87–89). These characteristics can be used to construct a correlation detector to identify Rayleigh waves in a seismic data stream.

We follow similar starting principles as Chael (1997) to construct our Rayleigh wave detector. Namely, we phase-advance the vertical channel by $\pi/2$ and correlate the result with a horizontal channel to look for high correlation values. In contrast to Chael (1997), we do not rotate the horizontal channel through a range of potential back azimuths – instead we assume a back azimuth consistent with a Blood Falls source and monitor for activity.

We exploit both tails of the correlation density function to monitor for Rayleigh waves traveling in opposite directions. A high absolute value of correlation between a horizontal channel and a Hilbert-transformed vertical channel indicates elliptically polarized particle motion in the plane defined by the horizontal and vertical channels. The sign of the correlation indicates the direction of wave travel. In a Blood Falls-centric reference frame: large positive values indicate waves traveling towards the seismometer from the Blood Falls direction, and large negative values indicate waves traveling away from the seismometer towards Blood Falls.

In order to detect statistically significant, retrograde elliptical particle motion indicative of Rayleigh waves, and save out the relevant data and event detection statistics, we performed the following operations.

1. We pre-processed the three-channel data for each station; we

(i) Detrended the data to remove the best straight-line fit from the data,

(ii) Filtered over 2.5–35 Hz with a bandpass, 4th order minimum phase Butterworth filter, and

(iii) Removed any samples for which data was not recorded on all three channels to equalize vector data length (required for subsequent matrix operations).

2. We rotated the seismogram data into a Blood Falls-centric horizontal reference system. Because we are interested in seismic sources near Blood Falls, we prescribed back azimuths to rotate the North (N) and East (E) channels into a radial (R) and transverse (T) orientation relative to Blood Falls using the equation:

$$\begin{bmatrix} R \\ T \end{bmatrix} = \begin{bmatrix} \cos\theta & \sin\theta \\ -\sin\theta & \cos\theta \end{bmatrix} \begin{bmatrix} N \\ E \end{bmatrix}, \tag{1}$$

where θ is the heading pointing from the seismometer towards Blood Falls, measured clockwise from the north (Incorporated Research Institutions for Seismology (IRIS), 2020). Rotation angle values used for θ are CECE: 330°, KRIS: 140°, and JESS: 70°. We performed a 2D rotation, since the seismometers are close together and we are interested in shallow, local sources.

3. We Hilbert transformed the vertical channel by performing a frequency independent phase advance of $\pi/2$.

4. We calculated cross-correlation between the aligned channel pair of the Hilbert-transformed vertical and radial channels, hereafter 'ZR'. The correlation process implemented a 0.75 second, tapered, sliding mid-point centered window.

5. We ran the correlation detector on both of the resulting ZR correlograms as follows:

(i) Correlograms were subset into 30-minute windows. For each 30-minute window, we: calculated the normalized data histogram based on the correlogram (e.g., the histogram in Figure 2b is calculated from the correlogram in Figure 2c), implemented MATLAB `normfit.m` to estimate the normal distribution parameters $\hat{\mu}$ (sample mean) and $\hat{\sigma}$ (sample standard deviation) of the middle 95% of the normalized data histogram, and calculated the fit error between this histogram and the theoretical PDF. The large-sample normality assumption for the correlation statistic is justified elsewhere (Wiechecki-Vergara et al., 2001).

(ii) Using the parameter estimates from the previous step, we calculated the probability density function (PDF) of the standard normal distribution evaluated at the same bin locations as the full data histogram.

(iii) We inverted the PDF to find the threshold corresponding to the desired CFAR and identified samples of the correlogram that exceed the detector threshold. In detail, we ran the detector with one-sided CFAR thresholds of $5 \text{x} 10^{-5}$ and $5 \text{x} 10^{-6}$. We calculated the threshold for both tails of the distribution separately for a given one-sided CFAR.

6. From the subset of threshold-exceeding correlation values identified in the previous step, we defined events. An event declaration required a minimum temporal separation from preceding or succeeding events (3.29 seconds). High correlation values with less temporal separation were grouped together. An event declaration also required at least 0.31 seconds duration between the first and final threshold exceedance (“trigger on” and “trigger off” times described in Figure 2d caption).

7. The highest correlation value and associated timestamp within the resulting block were saved as the event detection and time. We also calculated the p-value of the event detection statistic.

8. We ran the detector for each station for both tails in the ZR and ZT correlation distributions (corresponding to four source back azimuths per station) and for each of the two, one-sided CFAR thresholds. In this paper, we present the results corresponding to the right-tail of the ZR correlation distribution, 'ZR+', where events indicate waveforms traveling from the direction of Blood Falls toward the receiver. For simplicity, we refer to 'ZR+' as 'ZR' throughout this paper because we do not discuss the ZR- events.

We selected a minimum event duration of 0.31s based on visual inspection of waveforms detected under different duration requirements.

Text S3. Dominant Frequencies and Event Durations of Detected Rayleigh Events

To further investigate temporal variation in event duration and frequency throughout the year, we conduct the following analysis using the event catalogs generated by running the Rayleigh event detector. Each event catalog is defined as the collection of events identified from one station using a specific CFAR condition and back azimuth (ZR$\pm$ or ZT$\pm$, as defined by the preset rotation values, see Supporting Information Text S2). For instance: events identified at CECE with a back azimuth pointing towards the Blood Falls source region (ZR in Figure 2a) under a CFAR condition of 5x10^{-6} compose a catalog.

For each event identified by the detector under a specified CFAR condition, the duration of the event is defined as the total time elapsed between the first and final threshold exceedance within the event declaration (Figure 2d). Therefore, even if the same event is identified under multiple CFAR conditions, the event will have different event durations under different threshold conditions, and shorter durations will correspond to larger threshold values (lower CFAR values).

The dominant frequency within the passband ([2.5,35] Hz) for each event was calculated as follows: event start and end times from the detector output were used to extract seismogram data from the original SAC files. These data were then detrended, filtered, and rotated using the same methods as implemented in the event detector. We calculated the dominant frequency following Douma and Snieder (2006, equation 3).

Our examination of event detection rates did not point to any clear changes leading up to or coinciding with the initial visible brine release period. We also examined event duration and dominant frequency time series, but these characteristics likewise showed no changes we could clearly link with brine release. However, we did note differences between stations and seasons in dominant frequencies of detected events. The following analysis describes the variability of baseline changes in dominant frequencies throughout the observation period.

We plot dominant event frequency (on the vertical channel) against time of day in Figure S6, binned by month of year. Because our seismic experiment spanned November 2013–January 2015, a few month bins include data for more than one year, depending on station data availability. Darker colors represent events identified under smaller CFAR conditions (larger threshold values). As expected, more events are identified under the larger CFAR value.

At all stations, the dominant frequencies of detected Rayleigh events spans the passband ([2.5, 35] Hz), but visually cluster around certain frequency bands. Prominent examples include the strong horizontal bands between 20–30 Hz for land-based station CECE during March through October (Figure S6a). Dominant frequency patterns vary throughout the day during the summer. In particular, at on-ice station JESS in November (and to some extent in December), more events are detected and across a wider frequency band from 18:00–06:00 UTC; while from 06:00-18:00 UTC, dominant frequencies group toward the upper range of the passband (Figure S6c). A similar, but muted, pattern is apparent at CECE in November and December.

Text S4. Minimum Pulse Width and Phase Sensitivity

We demonstrate the minimum pulse width we could observe from a source about 500 m away given our experimental design (including our filter band, Nyquist frequency, and instrument response). To do this, we construct an internally consistent model that constrains the temporal width of a Rayleigh wave that is sourced at Blood Falls and recorded at our receiver 500 m away, after it dispersively attenuates through our half-space, 'lossy' model. We use the Futterman filter to provide this attenuation and dispersion, which has a frequency domain representation (Carmichael et al., 2015) of

$$e^{-t^*|\omega|/2+j\omega t^*/\pi \ln(|\omega|/2\pi f)} \tag{2}$$

where ω is angular frequency, t^* is travel time normalized by quality factor Q, j is the imaginary unit, $\ln(x)$ is the natural logarithm of argument x, and f is a reference frequency that we take to be the Nyquist frequency (100 Hz) of our sensor; smaller reference frequencies lead to more lossy mediums. To form this pulse, we propagated a delta-function signal from the source to the receiver with a Futterman filter (Futterman, 1962). We parameterized this filter with a quality factor of Q=40 (consistent with the attenuation value we use for the minimum detectable source size analysis in Section 3.3) and a Rayleigh wave speed of about 1.7 km/s. This is equivalent to the more common parameter representation that uses a t^* value (a key Futterman filter parameter) of $t^* = D/Qc_R$, where D is the distance between the source receiver and c_R is the Rayleigh wave speed. This operation dispersively attenuates the source pulse and thereby causally (or nearly so) broadens the pulse.

We then convolved this pulse with the L-22 geophone instrument response, which further broadens the pulse. In the absence of noise, such a pulse shows an apparent temporal width of about 0.4 s (blue arrows, Figure S9). The presence of noise would reduce this effective pulse width to be confined to the region that proceeds the large positive swing and includes the broader negative swing back to positive displacement (perhaps 0.2 s). We note that the units of counts on the vertical axis are arbitrary in the absence of noise.

However, we find that within that 0.4 s pulse duration that about 14 cycles fit at our highest frequency (35 Hz multiplied by 0.4 s; Figure S10), and about one full cycle fits at our lowest frequency (2.5 Hz multiplied by 0.4 s; Figure S11). Therefore, our Rayleigh wave detector will compare at waveforms with at least one full cycle because we require a minimum threshold exceedance of at least 0.31 s to declare an event.

Next, we consider the impact of phrase shift. As described above, we model the minimum duration pulse that propagates from a source located 500 m from a receiver. To do this, we propagate a delta function through our dispersively attenuating medium with a Futterman filter, and then convolve the instrument response of our L-22 receiver into this resulting pulse. We then produce a frequency modulated waveform within the passband of our 2.5 to 35 Hz filter by multiplying the resulting pulse model by a 10 Hz sinusoid. Next, we phase advance one of two copies of this signal by a set of phases between 45 and 135 degrees. We perform this phase advance by using Equation 5 in Box 5.6 from Aki and Richards (2009, p. 153) to express the phase advanced function as the original vertical channel signal, multiplied by the cosine of the phase shift, plus the Hilbert transform of the vertical channel signal, multiplied by the sine of the phase shift. Lastly, we injected these signals into noise such that the signal to noise ratio of the resultant seismograms, over their signal duration (0.4 s) was 10 (equivalent to 20 dB; Figure S12). This operation visibly produced a phase shift between the radial and vertical channels (Figure S13). We then computed the sample correlation coefficient between the radial channel seismogram and the transformed vertical channel seismogram to quantify how errors in the phase-advance assumption degraded our peak correlation coefficient (Figures S14 and S15). We compared these correlation coefficient detection statistics, as output by our Rayleigh wave detector, against the constant false alarm rate threshold ($5 \mathrm{x} 10^{-6}$); the correlation threshold was about 0.58 for these data. Our data show that the peak correlation coefficient remains above this threshold, even when the phase error is as absolutely large as 45°; this appears to inconsistently trigger our detector according to our trigger criteria. We also note that a positive phase error (so that the phase shift is +135°rather than -45°) leads to larger peak correlation coefficients. Therefore the errors are asymmetric, and negative errors relative to 90°could lead to more Rayleigh wave correlation detection losses when compared to positive errors.

Text S5. Source Depth Analysis

We perform the following analysis to estimate the maximum potential Rayleigh-wave generating source depths we sample with the frequencies used in our seismic experiment. Sources deeper than this estimate could evade detection, given our experimental design (including factors like receiver locations and frequencies used in our seismic experiment).

In doing so, we estimate the source size required to produce a waveform of a given amplitude at a receiver location. Our solution is approximate, and uses results from Chapter 7, Aki and Richards (2009). In particular, we generate half-space eigenfunctions, but use dispersive relationships present in a layer–over–half-space.

In our layer–over–half-space configuration, the top 50 m thick layer represents the cold ice of Taylor Glacier and the half-space represents the subglacial basement. Widespread, saline-saturated sediments are known to exist beneath Taylor Glacier; the thickness of this layer under the terminal kilometer of the glacier is on the order of at least tens of meters (Mikucki et al., 2015, Figure 3). We do not include this layer in our model. We further make the simplifying assumption that the glacier ice is homogeneous, in contrast to the more complicated reality of a stiff, relatively clean ice layer overlying a much more deformable, debris-rich basal ice layer (Pettit et al., 2014).

We use the same model input values as a prior seismic study at Taylor Glacier (Carmichael et al., 2012), which was informed by an active seismic survey conducted in nearby Beacon Valley (Shean et al., 2007). Specifically, we use p-wave and s-wave speeds of 3850 m/s and 1950 m/s for the ice layer and 4800 m/s and 2900 m/s for the substrate half-space. We use a standard ice density of 917 kg/m^3 and a substrate density of 2700 kg/m^3 consistent with basement velocities in Taylor Valley (Table 1, Barrett & Froggatt, 1978, and references therein).

Following Aki and Richards (2009, p. 328), we solve for Rayleigh wave displacement using

$$\mathbf{u}^{\mathrm{RAYLEIGH}}(\mathbf{x},\omega) = \mathbf{G^R}[U_1 + U_2\cos(2\phi) + U_3\sin(2\phi)], \tag{3}$$

where $\mathbf{u}^{\mathrm{RAYLEIGH}}$ is the displacement, dependent on the source-receiver distance ($\mathbf{x}$) and angular frequency (ω). $\mathbf{G^R}$ is the azimuthally-independent displacement vector described below. Coefficients U_1, U_2, and U_3 describe the radiation pattern, with azimuthal angle ϕ between the source and receiver. We use the radiation pattern for a crack opening in the direction of the receiver to maximize the total displacement. We refer the reader to Carmichael (2021, equation 39) and Carr, Carmichael, Pettit, and Truffer (2020, Appendix C) for further documentation of the radiation pattern specific to the crack opening.

We solve for the eigenfunction $r_1(h)$ in the azimuthally-independent displacement vector (Aki & Richards, 2009, p. 328):

$$\mathbf{G^R}(\mathbf{x};h,\omega) = \sum_n \frac{k_n r_1(h)}{8cUI_1} \sqrt{\frac{2}{\pi k_n r}}\; e^{\left[i\left(k_n r - \frac{\pi}{4}\right)\right]}\; [r_1(z)\hat{\mathbf{r}} + ir_2(z)\hat{\mathbf{z}}], \tag{4}$$

where $r_1(h)$ is horizontal displacement at the unknown source depth h. We use eigenfunctions $r_1(z)$ and $r_2(z)$ (vertical displacement) for the half-space below the surface layer for each term in the sum, and populate their exponential arguments with the wave number k_n from the dispersion relationship (previously calculated for the minimum detectable event size analysis, see Section 3.3 in the main text). Other terms in equation 4 include: phase velocity $c = \omega/k_n$ (angular frequency divided by wave number), group velocity U, and energy integral I_1 (for a full description, see Carmichael (2021) and Appendix C in

Carr et al. (2020)). Figure S17 shows the displacement for the r_1 and r_2 eigenvectors for frequencies of 2.5 and 35 Hz.

To relate the correlation coefficient output by the Rayleigh wave detector to the threshold source size, we use the relationships between signal-to-noise ratio (SNR), the sample correlation, and the target waveform amplitude. We first note that the SNR of a noisy signal is representable as the correlation coefficient ρ between waveforms of the same shape:

$$\mathrm{SNR} = \frac{\rho}{1-\rho}. \tag{5}$$

where ρ, in this case, is the value of the correlation threshold required for a meaningful detection (defined by a specific CFAR condition) and SNR is the square of the Rayleigh waveform amplitude, divided by the noise energy. The noise energy is the estimated sample variance $\hat{\sigma}^2$ multiplied by one less the number of samples $(N-1)$ in the Rayleigh wave detector window:

$$\mathrm{SNR} = \frac{||\mathbf{u}^{\mathrm{RAYLEIGH}}||^2}{\hat{\sigma}^2(N-1)}. \tag{6}$$

We substitute equation 6 into equation 5 to relate threshold Rayleigh wave size (numerator of equation 6) to the estimated noise variance and correlation threshold. We approximate $\mathbf{u}^{\mathrm{RAYLEIGH}}$ using the content on page 328 of Aki and Richards (2009) described above (equation 3), which then provides a relationship between $r_1(h)$ (a function of source depth) and the estimates from the data. The equality that outputs source depth therefore includes analytical formulation; numerical calculation of the dispersion relationships to compute phase velocity c, group velocity U, and the wavenumber versus frequency relationship (k_n); and both noise and deterministic parameter estimates from the data ($\hat{\sigma}^2$, ρ and N).

We selected the same three weeks (10-30 May 2014) used in the prior detector threshold analyses, calculated sample variance from the pre-processed (detrended, filtered, rotated) data, and extracted detector thresholds from the Rayleigh detector results under the $5\text{x}10^{-6}$ CFAR condition (Table S1).

We chose the values from Table S1 for each station that would provide the shallowest source for the detection limit, namely: the largest threshold and highest sample variance. For all stations, we find that sources depths shallower than about 2.5 km produce displacement above the detection limit. Specifically, for land-based stations CECE the threshold detection depth is 2.9 km, at KRIS the threshold detection depth is 2.6 km and for on-ice station JESS the threshold detection depth is 2.5 km. We conclude that our Rayleigh wave detector would trigger on elliptically polarized waveform data sourced by a crack emplaced at shallower depths than ∼2.5 km in the observed noise environment.

Text S6. Description of Additional Figures

A large crack in the glacier surface was visible following the winter 2014 brine release (Figure S1). This photo from 21 November 2014 shows the brine icing largely intact, with some incised meltwater channels. The lake ice and moat appear to be still frozen.

We generated spectrograms from the seismic data in order to perform a visual data quality check and to qualitatively investigate potential relationships between meteorological variables and spectral features. Spectrograms were generated from the detrended, bandpass-filtered ([2.5, 35] Hz) data using 8 second windows with 5 second overlap. For this initial analysis, we did not remove the instrument response; therefore, the units are related to amplitude in counts rather than ground displacement or velocity.

In Figures S2, S3, and S4, temperature (left y axis) and wind speed (right y axis) are plotted on the upper panel of each subplot; scales vary from month to month to accommodate seasonality. Meteorological data are from the Taylor Glacier station (Doran & Fountain, 2019). The three channels (EHZ: vertical, EHE: East, and EHN: North) are plotted in the lower three panels of each subplot.

We visually inspected spectrograms to identify time periods when data quality was poor, and excluded these days from the Rayleigh wave detection analysis. Examples include data from station CECE prior to servicing in January 2014 (Figure S2a) and station JESS after 9 December 2014 (Figure S4b). During the onset of brine release in May 2014 (Figure S3), we deemed data quality on all channels at all stations to be sufficient for the Rayleigh wave analysis. Examples of detected waveforms are included in Figure S5.

In Figures S6, S7, and S8 we plot dominant frequency of identified Rayleigh wave events arriving at each seismic station from a Blood Falls back azimuth against time of day (Figures S6) or the event duration (Figures S7 and S8). Dominant frequency and event duration are calculated as described in the Text S3 above. In Figure S7, each station's subplot includes all data for all identified Rayleigh events, while in Figure S8 the events are separated by month of year. Event duration clusters strongly around 0.6–0.7 seconds, and the distribution of event times is skewed to the left (shorter event duration) with a long right-hand (longer event duration) tail. The clustering of event times suggests a repetitive source with a given physical dimension.

Figures S9–S15 are described in Text S4 above.

Our Rayleigh detector exploited both tails of the statistical distribution as well as correlation between the vertical and transverse channels (with respect to a Blood Falls back azimuth) to detect Rayleigh events arriving from other directions. We plot results from one back azimuth, the ZR back azimuth, representing Rayleigh waves traveling from Blood Falls to the sensor in Figure S16 (see Figure 2 for back azimuth directions). The lighter shade of blue on each time series are the event detection rates for a CFAR of $5\text{x}10^{-5}$; the bold lines are the detection rates with a CFAR of $5\text{x}10^{-6}$. The initial Blood Falls brine release is highlighted in red for the CFAR = $5\text{x}10^{-6}$ results on all plots.

A meteorological station (Doran & Fountain, 2019) located on Taylor Glacier collected air temperature and wind speed during the duration of our seismic experiment (Figure S16g). A previous study at Taylor Glacier modeled melt occurring at temperatures as low as −2.7°C during the summer season due to solar radiation (Hoffman et al., 2008). However, the brine release events documented in our study occurred when air temperatures were well below this threshold; therefore, we assume negligible surface melt. Air temperatures at the Lake Bonney meteorological station (located on dark rocks and sediment on the south shore of Lake Bonney) follow a similar pattern and are slightly warmer yet still subfreezing. Warm air temperature spikes during winter months correspond with increases in wind speed (Nylen et al., 2004; Speirs et al., 2010).

In Figure S17, the normalized vertical and horizontal displacement for the Rayleigh eigenfunctions associated with our source model from Text S5 above are plotted as a function of depth. As described in Text S5, we used the detector threshold values and sample variance from Table S1 as input values to constrain our source depth model.

Various cracks in ice are present in the environment near the glacier terminus (Figure S18), including ice blisters (Figure S19). The approximate scale of these cracks ranges from tens of centimeters to several meters in length, with openings on the order of centimeters to tens of centimeters.

Movie S1. Movie created from time-lapse photos, one image per day from 9 May 2014 – 7 June 2014. See Text S1 above for an explanation of the time zone correction we applied; all time stamps are given in our best estimate of UTC time. File name: ms01.mp4.

Movie S2. Movie created from time-lapse photos, one image per 2 hours except when power loss interrupted data collection. Note the movie retains a placeholder of the most recently available image while the counter in the lower left advances, these frames are labeled like "no data, image from 08-Jun-2014 16:47 UTC". See Text S1 above for an explanation of the time zone correction we applied; all time stamps are given in our best estimate of UTC time. File name: ms02.mp4.

References

Aki, K., & Richards, P. G. (2009). *Quantitative Seismology* (Second ed.). Mill Valley, CA, USA: University Science Books.

Barrett, P. J., & Froggatt, P. C. (1978). Densities, porosities, and seismic velocities of some rocks from Victoria Land, Antarctica. *New Zealand Journal of Geology and Geophysics*, *21*(2), 175–187. doi: 10.1080/00288306.1978.10424049

Carmichael, J. D. (2021). Hypothesis tests on Rayleigh wave radiation pattern shapes: a theoretical assessment of idealized source screening. *Geophysical Journal International*, *225*(3), 1653–1671. doi: 10.1093/gji/ggab055

Carmichael, J. D., Joughin, I., Behn, M. D., Das, S., King, M. A., Stevens, L., & Lizarralde, D. (2015). Seismicity on the western Greenland Ice Sheet: Surface fracture in the vicinity of active moulins. *Journal of Geophysical Research F: Earth Surface*, *120*(6), 1082–1106. doi: 10.1002/2014JF003398

Carmichael, J. D., Pettit, E. C., Hoffman, M., Fountain, A., & Hallet, B. (2012). Seismic multiplet response triggered by melt at Blood Falls, Taylor Glacier, Antarctica. *Journal of Geophysical Research: Earth Surface*, *117*(F3), 16 pp. doi: 10.1029/2011JF002221

Carr, C. G., Carmichael, J. D., Pettit, E. C., & Truffer, M. (2020). The influence of environmental microseismicity on detection and interpretation of small-magnitude events in a polar glacier setting. *Journal of Glaciology*, *66*(259), 790–806. doi: 10.1017/jog.2020.48

Chael, E. P. (1997). An automated Rayleigh-wave detection algorithm. *Bulletin of the Seismological Society of America*, *87*(1), 157–163.

Doran, P. T., & Fountain, A. G. (2019). *McMurdo Dry Valleys LTER: High frequency measurements from Taylor Glacier Meteorological Station (TARM) in Taylor Valley, Antarctica from 1994 to present.* Environmental Data Initiative. doi: 10.6073/pasta/a1df5cdab3319e9adeb18f8448fd363e

Douma, H., & Snieder, R. (2006). Correcting for bias due to noise in coda wave interferometry. *Geophysical Journal International*, *164*(1), 99–108. doi: 10.1111/j.1365-246X.2005.02807.x

Futterman, W. I. (1962). Dispersive body waves. *Journal of Geophysical Research*, *67*(13), 5279-5291. doi: 10.1029/JZ067i013p05279

Hoffman, M. J., Fountain, A. G., & Liston, G. E. (2008). Surface energy balance and melt thresholds over 11 years at Taylor Glacier, Antarctica. *Journal of Geophysical*

Research, *113*(F4), 12 pp. doi: 10.1029/2008JF001029

Incorporated Research Institutions for Seismology (IRIS). (2020). *IRIS DMC IRISWS rotation Web Service Documentation.* http://service.iris.edu/irisws/rotation/1/.

Mikucki, J. A., Auken, E., Tulaczyk, S., Virginia, R. A., Schamper, C., Sørensen, K. I., ... Foley, N. (2015). Deep groundwater and potential subsurface habitats beneath an Antarctic dry valley. *Nature Communications*, *6*(6831), 9 pp. doi: 10.1038/ncomms7831

Nylen, T. H., Fountain, A. G., & Doran, P. T. (2004). Climatology of katabatic winds in the McMurdo Dry Valleys, southern Victoria Land, Antarctica. *Journal of Geophysical Research*, *109*(D03114), 9 pp. doi: 10.1029/2003JD003937

Pettit, E. C., Whorton, E. N., Waddington, E. D., & Sletten, R. S. (2014). Influence of debris-rich basal ice on flow of a polar glacier. *Journal of Glaciology*, *60*(223), 989–1006. doi: 10.3189/2014JoG13J161

Shean, D. E., Head III, J. W., & Marchant, D. R. (2007). Shallow seismic surveys and ice thickness estimates of the Mullins Valley debris-covered glacier, McMurdo Dry Valleys, Antarctica. *Antarctic Science*, *19*(4), 485–496. doi: 10.1017/S0954102007000624

Speirs, J. C., Steinhoff, D. F., McGowan, H. A., Bromwich, D. H., & Monaghan, A. J. (2010). Foehn winds in the McMurdo Dry Valleys, Antarctica: the origin of extreme warming events. *Journal of Climate*, *23*(13), 3577–3598. doi: 10.1175/2010JCLI3382.1

Stein, S., & Wysession, M. (2003). *An Introduction to Seismology, Earthquakes, and Earth Structure.* Malden, MA, USA: Blackwell Publishing.

Wiechecki-Vergara, S., Gray, H. L., & Woodward, W. A. (2001). *Statistical Development in Support of CTBT Monitoring.* Dallas, TX, USA: Southern Methodist University.

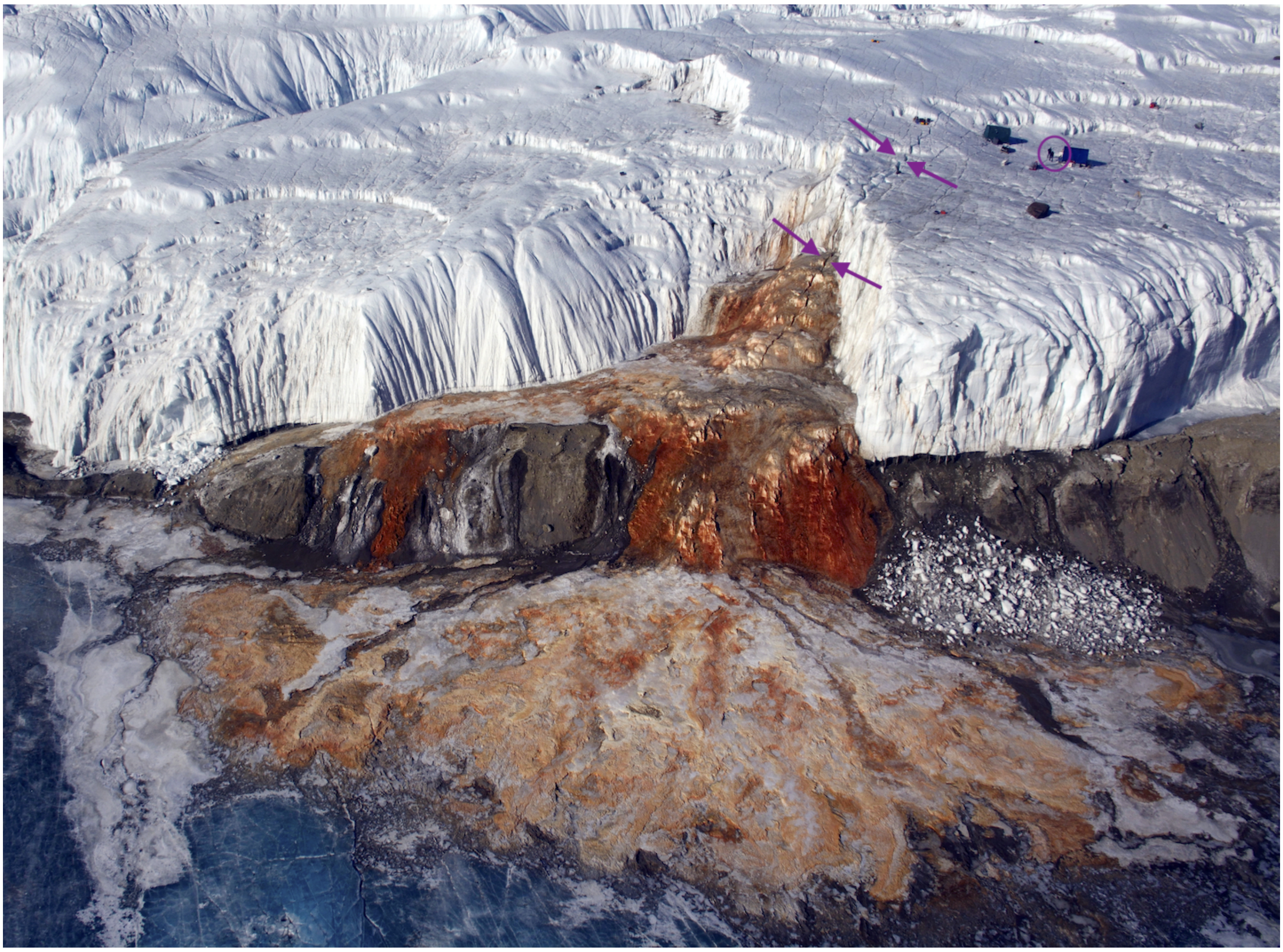

Figure S1. Taylor Glacier terminus following the winter 2014 brine release event. Two sets of purple arrows mark the Blood Falls crevasse; for scale, two people are circled in purple standing next to tents on the glacier surface. Photo: Peter Rejcek, photo date: 21 November 2014. Photo source: National Science Foundation US Antarctic Program Photo Library (https://photolibrary.usap.gov).

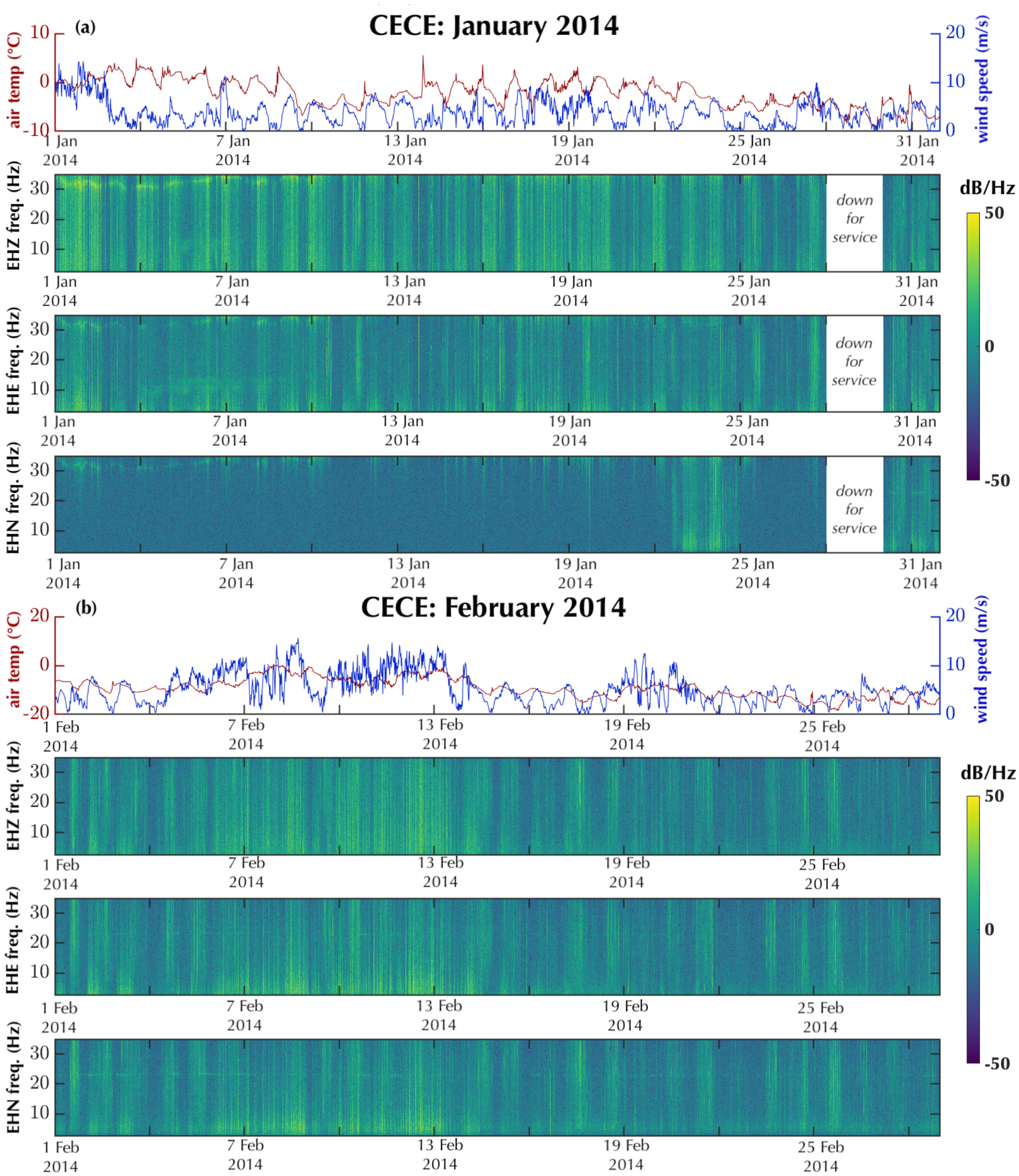

Figure S2. Spectrograms for station CECE for (a) January 2014 and (b) February 2014. Prior to instrument servicing 29 Jan 2014, the north channel (EHN) was not operating properly; the issue was corrected during servicing.

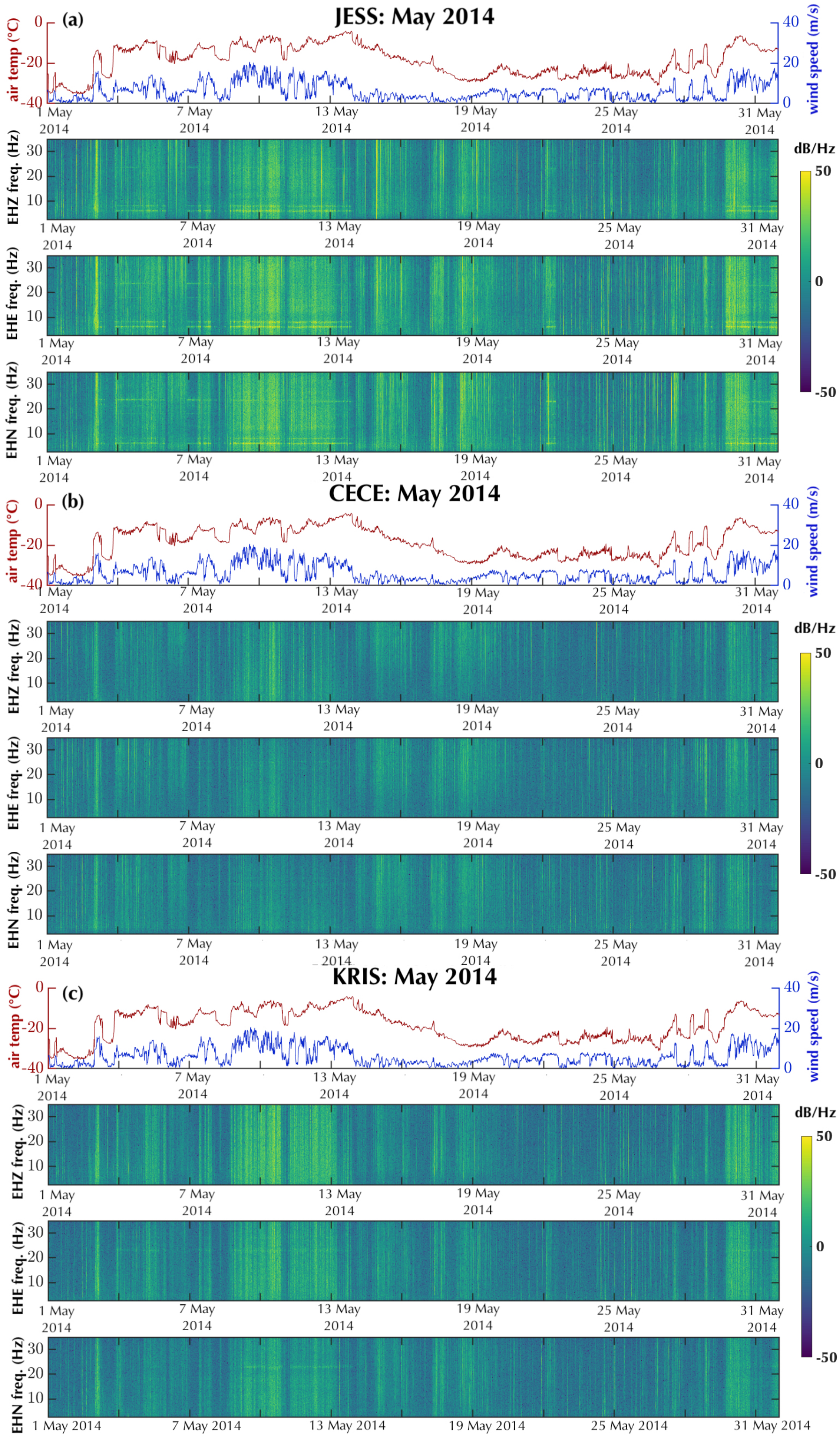

Figure S3. Spectrograms for all stations for May 2014: (a) JESS, (b) CECE, and (c) KRIS.

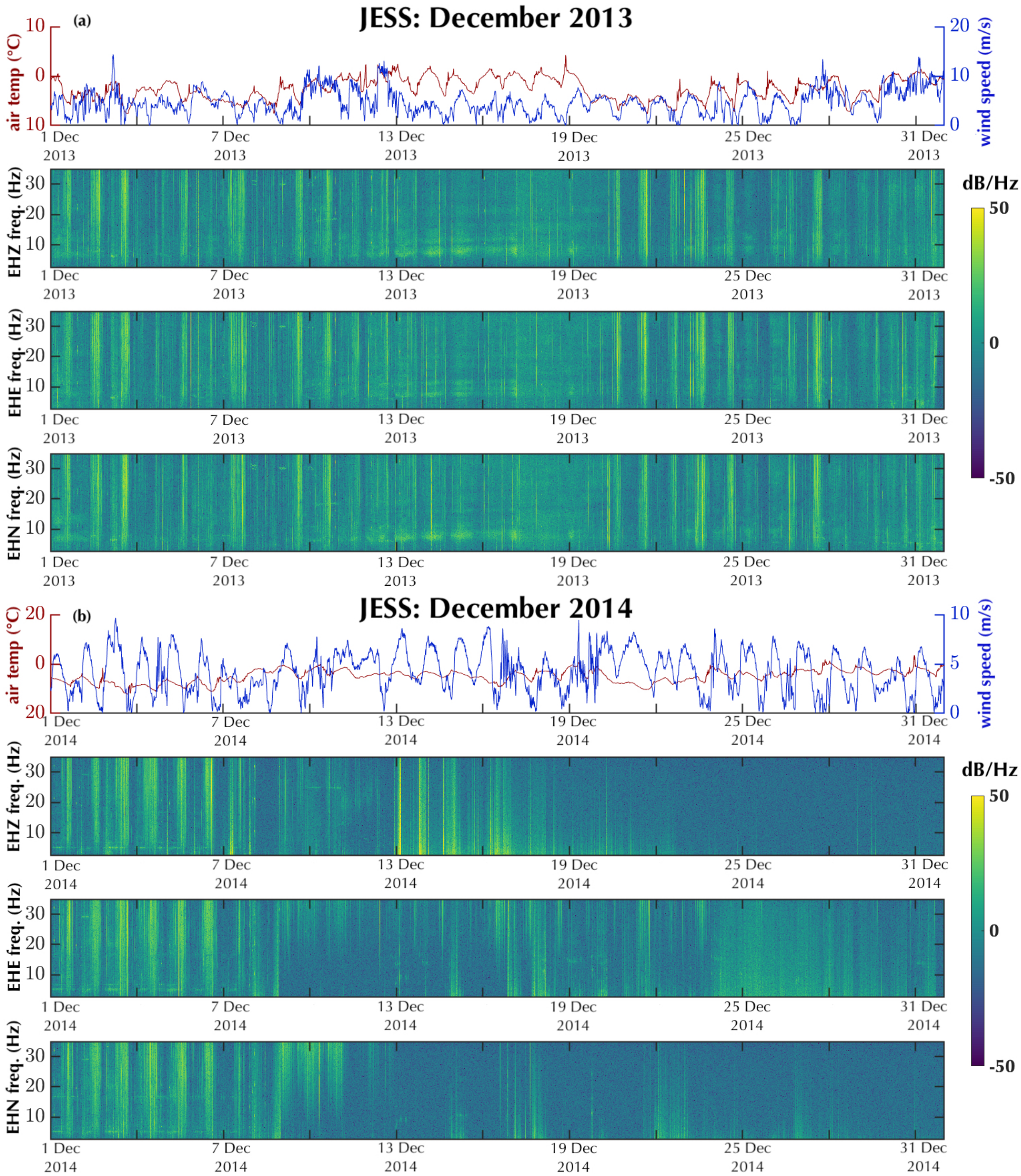

Figure S4. Spectrograms for station JESS for (a) December 2013 and (b) December 2014. During the second week of December 2014, data quality rapidly declines and never improves. Note different scales for temperature and wind speed for the two subplots.

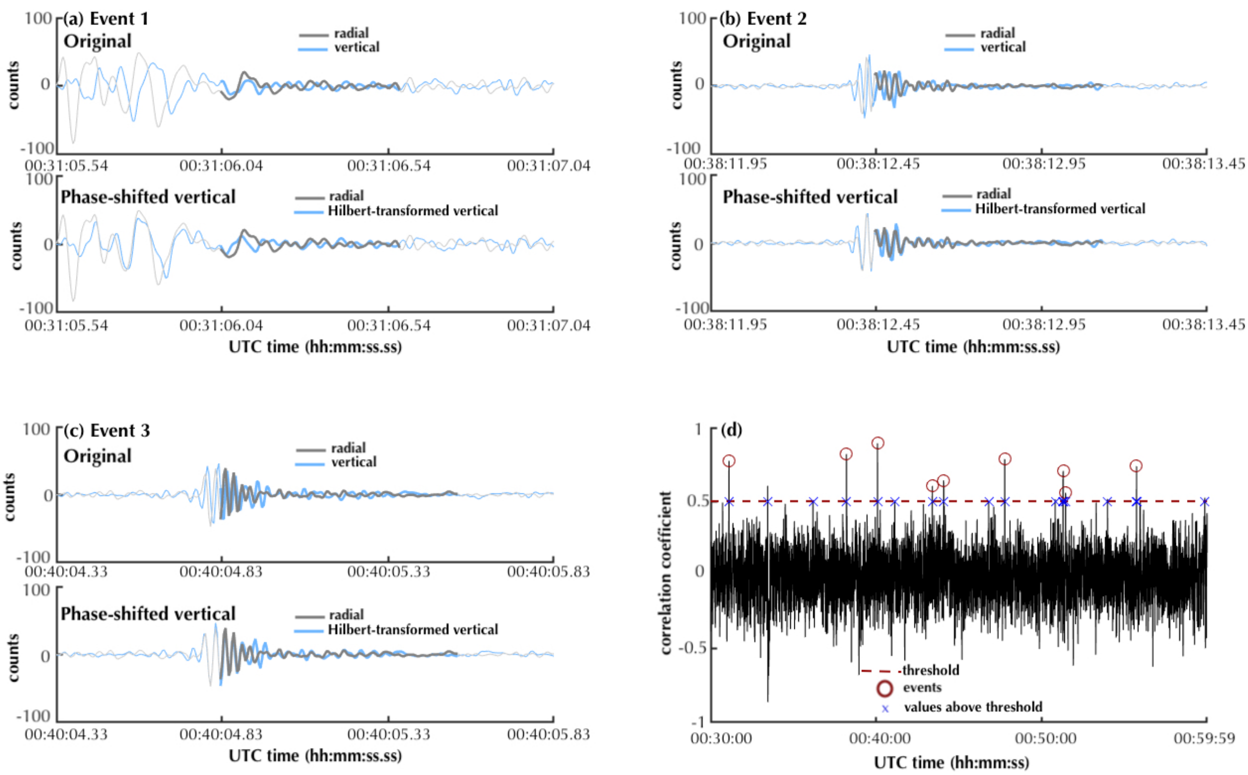

Figure S5. Example waveforms from station CECE on 20 March 2014. In (a)–(c), the upper plot shows the original radial and vertical channels, and the lower plot shows the original radial and phase-shifted vertical channel. The portions of the waveform that triggered the detector are bolded. Event numbers 1-3 correspond to the first three circles in (d). In (d) the Rayleigh wave detector correlation coefficient is plotted for the full 30-minute window. Note different horizontal axes: (a)–(c) span 1.5 seconds, while (d) spans 30 minutes.

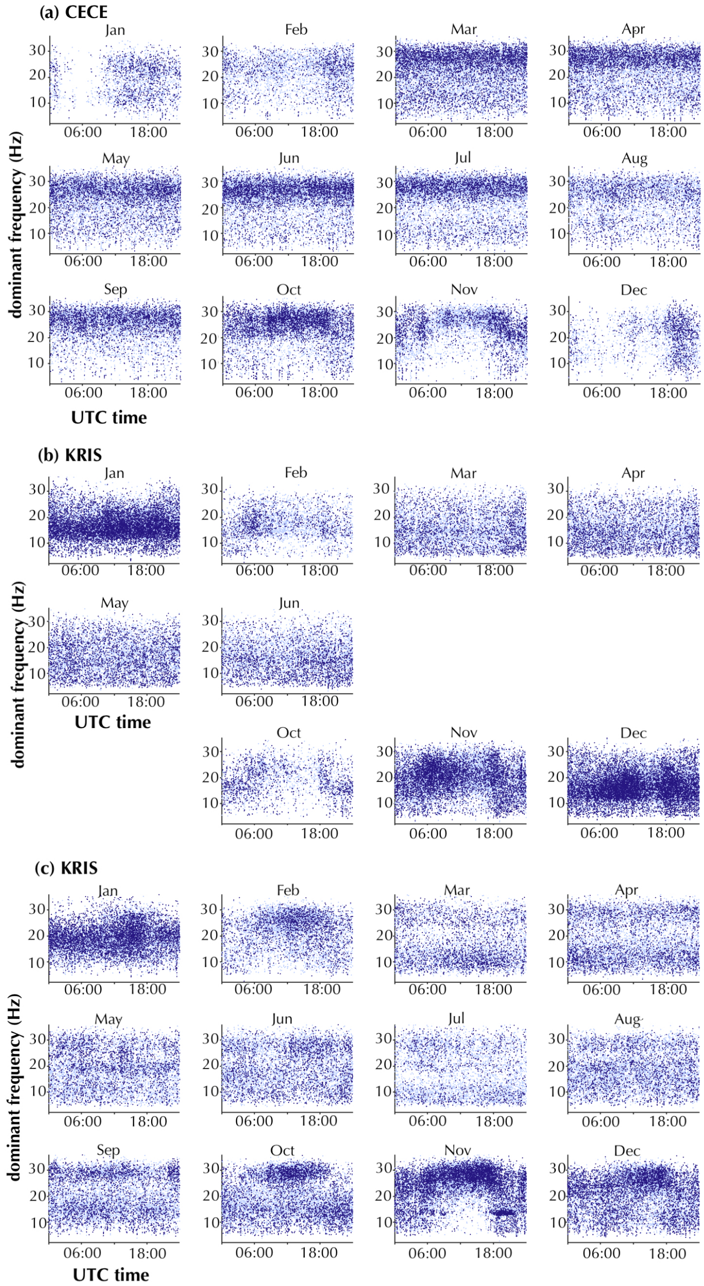

Figure S6. Dominant frequencies of vertical channel data recorded on each station during Rayleigh events (vertical axis, all subplots) and plotted against event time of day (time of day in UTC for all subplots), for a back azimuth oriented towards Blood Falls. Darker data points represent the smaller CFAR value (larger threshold values). Plots for some station/month pairs include data from multiple years. Note all plots have the same axes scales, but some labels are suppressed for readability.

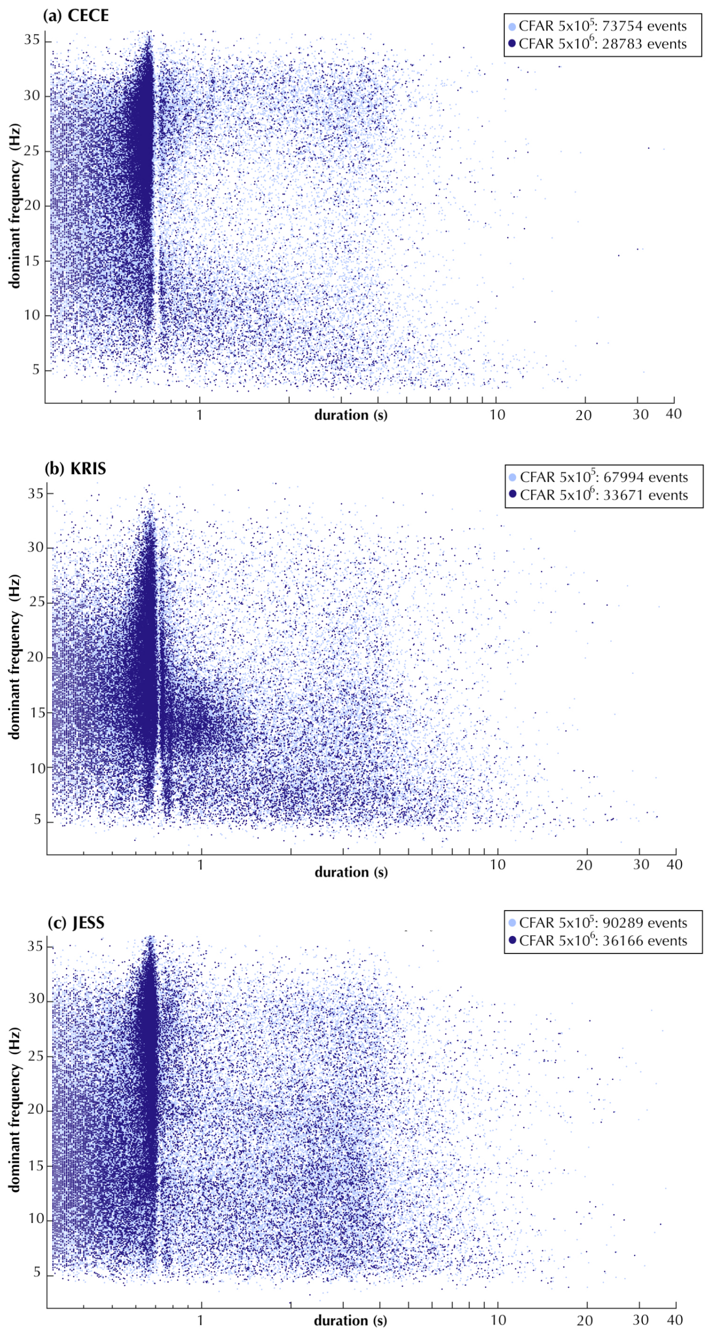

Figure S7. Dominant frequency on the vertical channel and event duration (log scale) for Rayleigh events identified with a Blood Falls back azimuth from each station. Darker colors indicate the smaller CFAR value (higher threshold values). The legend for each plot lists the number of events identified under each CFAR condition, summed over the entire data period.

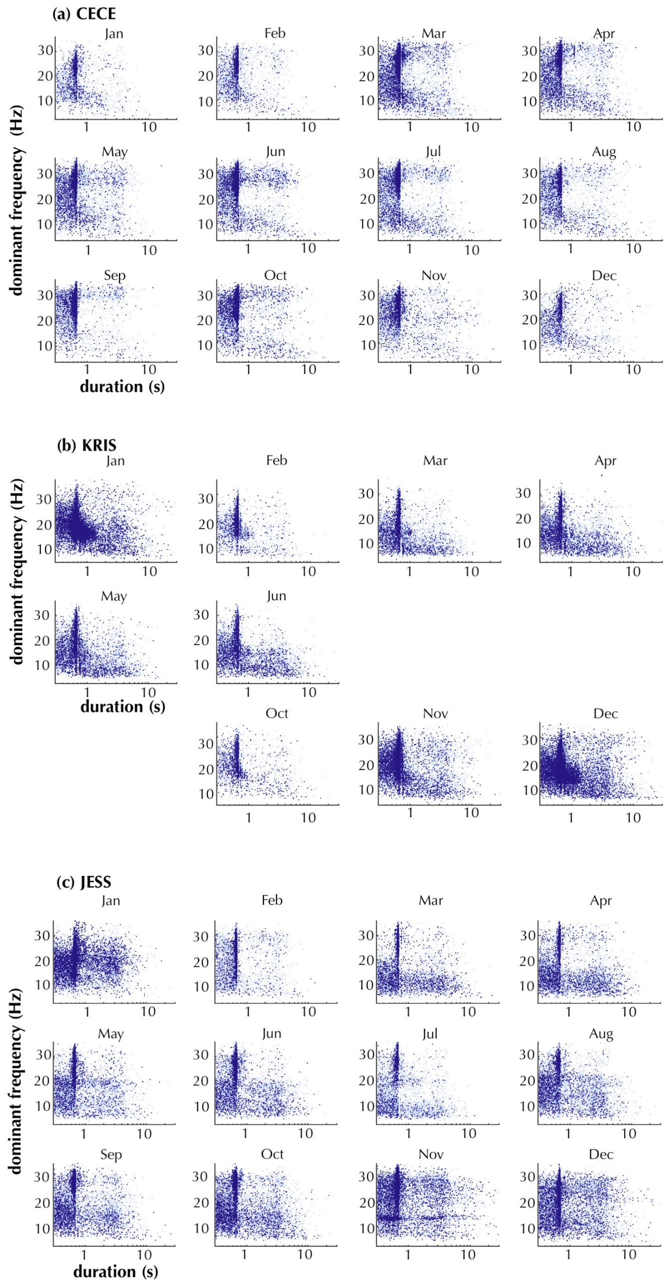

Figure S8. Dominant frequency on the vertical channel during Rayleigh events (vertical axis, all subplots) and event duration (horizontal axis, all subplots) for Blood Falls back azimuth events for each station. Event duration is plotted on a log scale. Darker data points represent the smaller CFAR value (larger threshold values). Plots for some station/month pairs include data from multiple years. Note all plots have the same axes scales, but some labels are suppressed for readability.

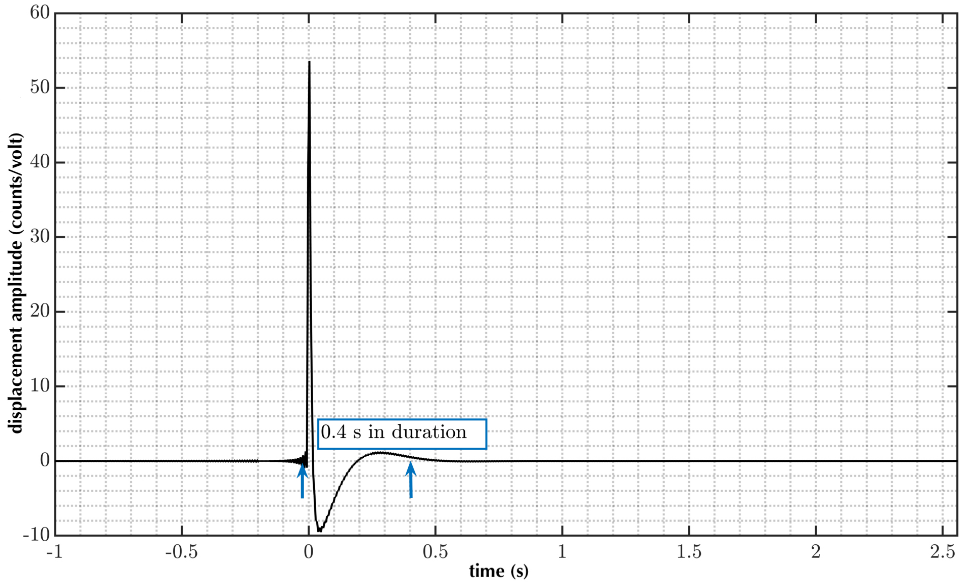

Figure S9. Pulse as observed by a receiver 500 m from the source. To form this pulse, we propagated a delta-function signal from the source to the receiver, with a Futterman filter (Futterman, 1962). We used the following values for the filter parameter $t* = D/Qc_R$: distance ($D = 500\,\mathrm{m}$), quality factor ($Q = 40$), and Rayleigh wave speed ($c_R = 1.7\,\mathrm{km/s}$). This operation dispersively attenuates the source pulse and thereby causally (or nearly so) broadens the pulse. We then convolved this pulse with the L-22 geophone instrument response, which further broadens the pulse. In the absence of noise, such a pulse shows an apparent temporal width of about 0.4 s (blue arrows). The presence of noise would reduce this effective pulse width to be confined to the region that proceeds the large positive swing and includes the broader negative swing back to positive displacement (perhaps 0.2 s). The counts values on the vertical axis are arbitrary in the absence of noise.

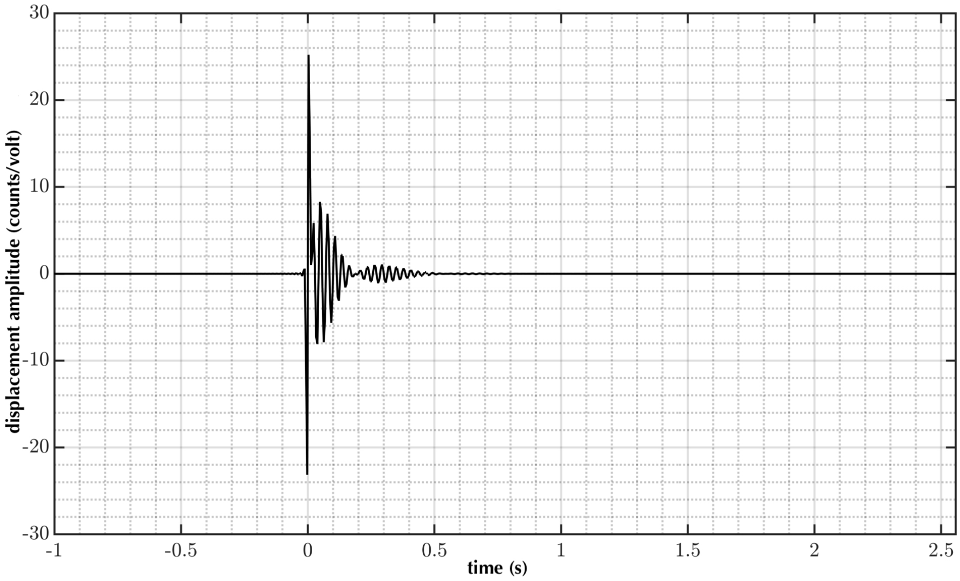

Figure S10. Same as Figure S9, but with a 35Hz source time function superimposed onto the pulse. While the y-scale differs from Figure S9, the counts values on the vertical axis are arbitrary in the absence of noise.

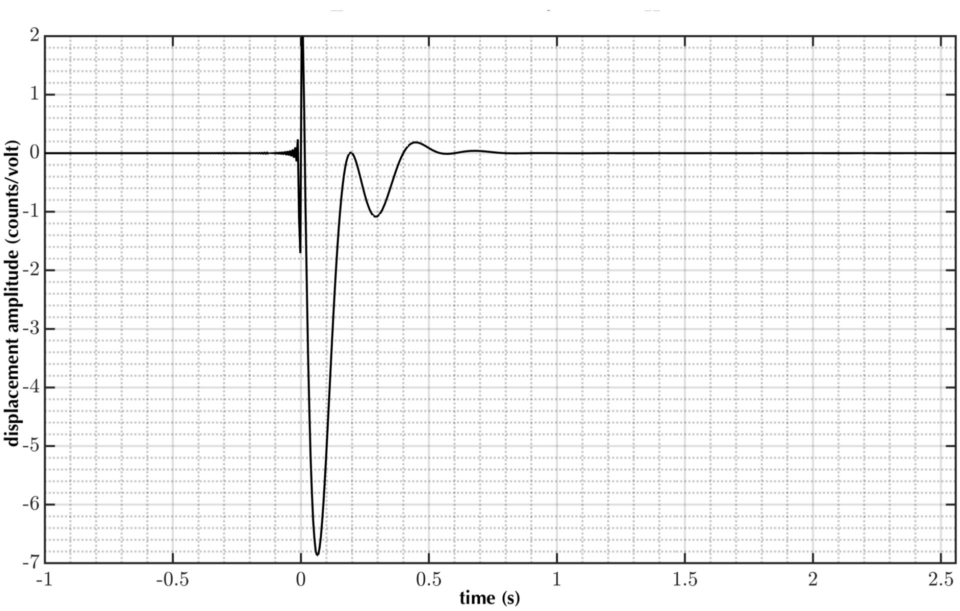

Figure S11. Same as Figure S9, but with a 2.5 Hz source time function superimposed onto the pulse. While the y-scale differs from Figure S9, the counts values on the vertical axis are arbitrary in the absence of noise.

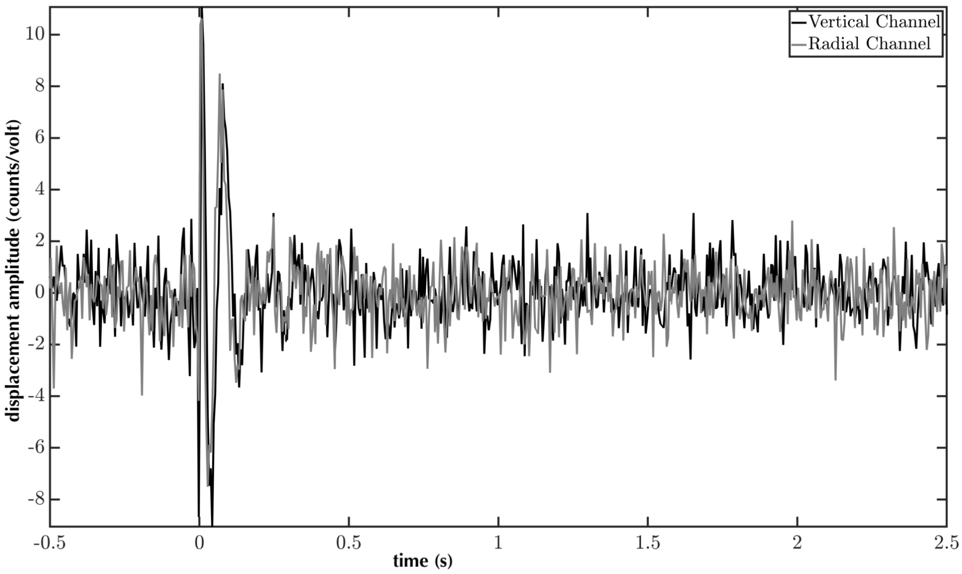

Figure S12. A vertical channel seismogram, phase advanced by 135°(black) compared against a radial channel seismogram (grey).

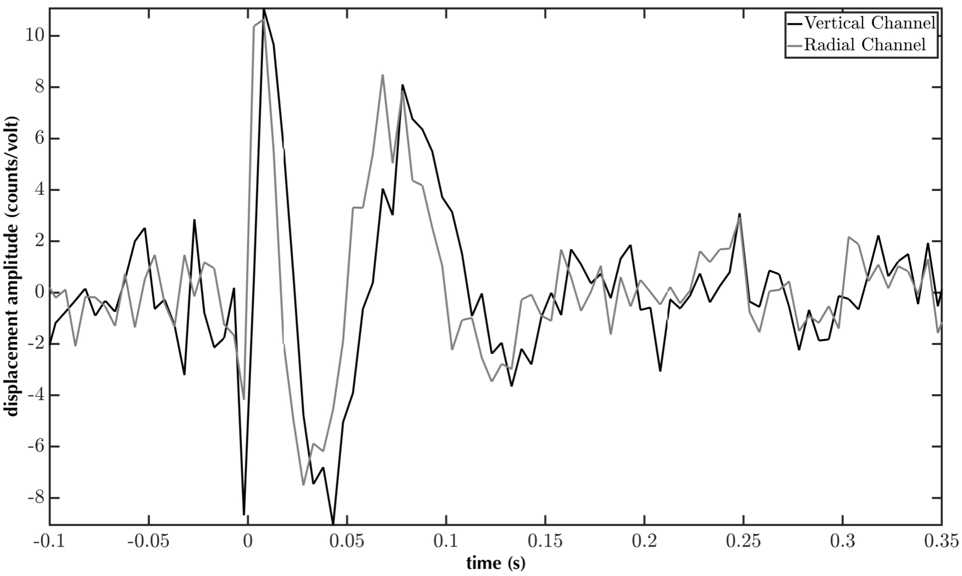

Figure S13. Same as Figure S12, but zoomed in between -0.1 s and 0.35 s to illustrate the visible phase difference.

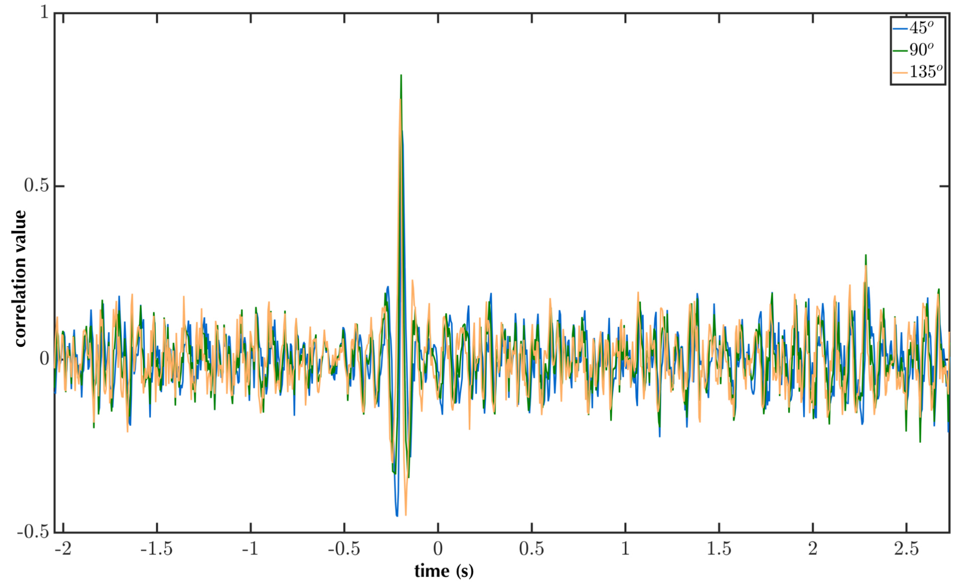

Figure S14. Sample correlation coefficient time series that show the output of a Rayleigh wave detector when the vertical channel seismogram is phase shifted relative to the radial seismogram (phase shifts shown in legend). The vertical axis shows the sample correlation coefficient and is bounded between -1 and 1.

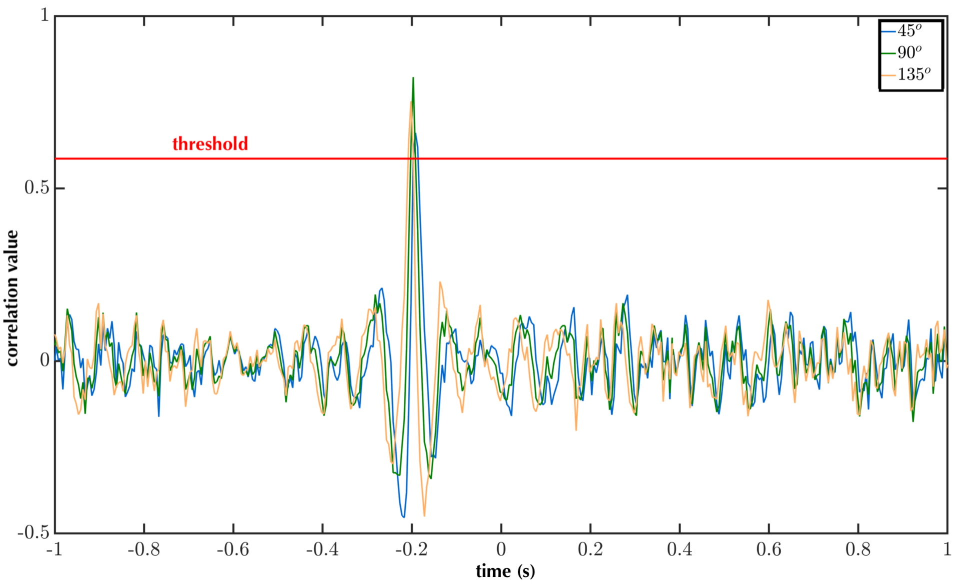

Figure S15. Same as Figure S14, but zoomed in over time -1 to 1 and shown with a threshold for detection that is consistent with the false alarm constraint. The vertical axis shows the sample correlation coefficient and is bounded between -1 and 1, as in Figure S14.

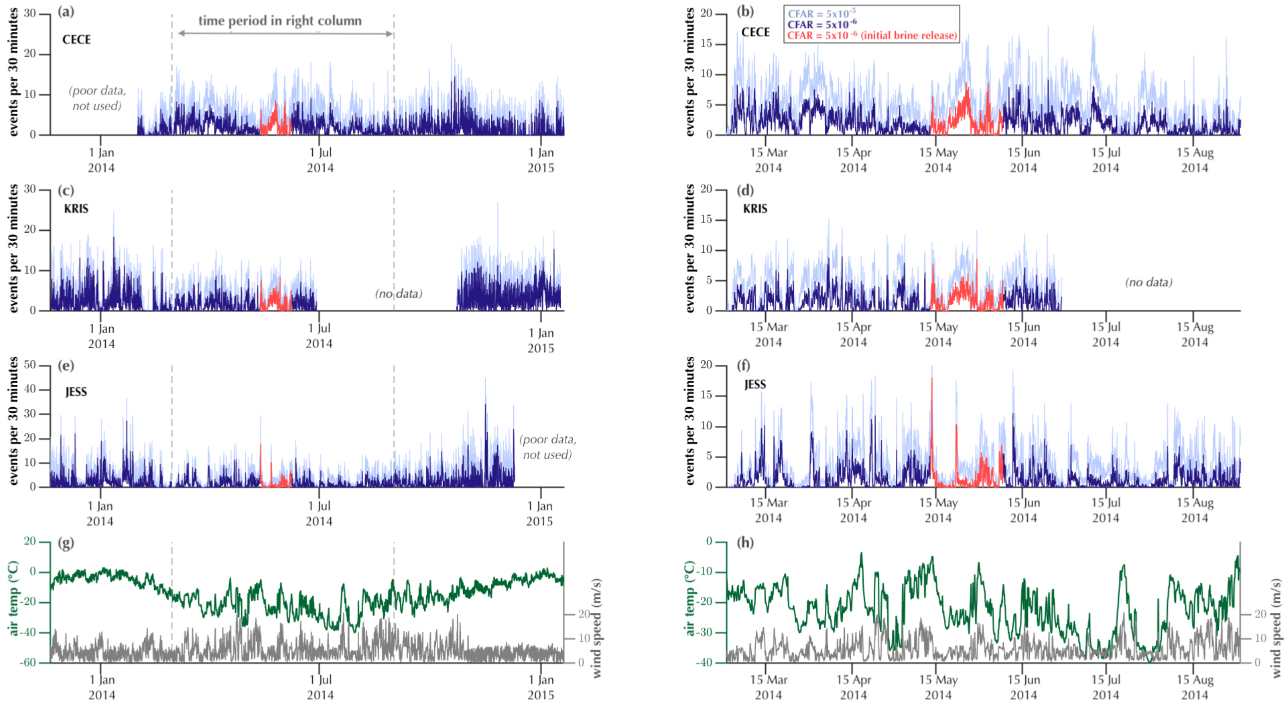

Figure S16. Events per 30 minutes, as identified by the Rayleigh-wave detector at (a, b) land-based station CECE, (c, d) land-based station KRIS (power failure caused data loss after June 30), and (e, f) on-ice station JESS (for this station, in the detail panel (d) only, some rates above 20 events per 30 minutes identified using the 5x10^{-5} CFAR are cut off by the vertical scale). Note different vertical scales on panels (a), (c), and (e). The CFAR = 5x10^{-6} condition is highlighted in dark blue and red (red indicates initial visible brine release period 13 May – 8 June 2014), and the 5x10^{-5} CFAR condition results are in light blue to show the range in detected event rates. In (g, h), air temperature (green, left vertical axis) and wind speed (gray, right vertical axis) from the nearby Taylor Glacier meteorological station (Doran & Fountain, 2019) are plotted. All time series are smoothed with a 2-hour duration (event detection rates: 5-point, weather data: 9-point) moving window.

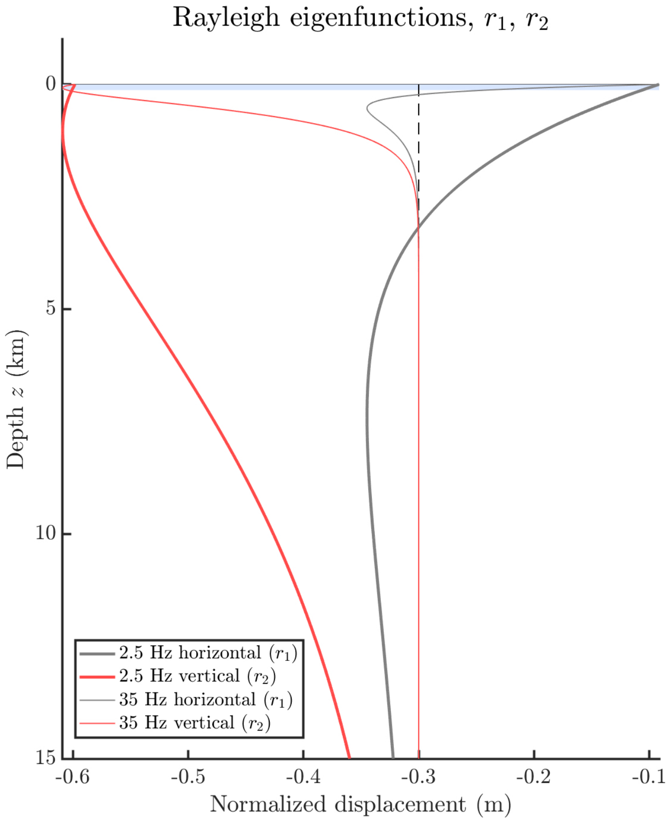

Figure S17. Frequency-dependent, normalized vertical and horizontal displacement as a function of depth, calculated for the eigenfunctions described in the text. The light blue layer represents the 50 m-thick glacier in our model.

Figure S18. Various cracks in ice near the glacier terminus. Cracks include crevasses on the glacier near the cliff face, cracks in the ice-cored terminal moraine (sediment at left of photo), and in the lake ice where the person is standing. Photo: Chris Carr, photo date: November 2013.

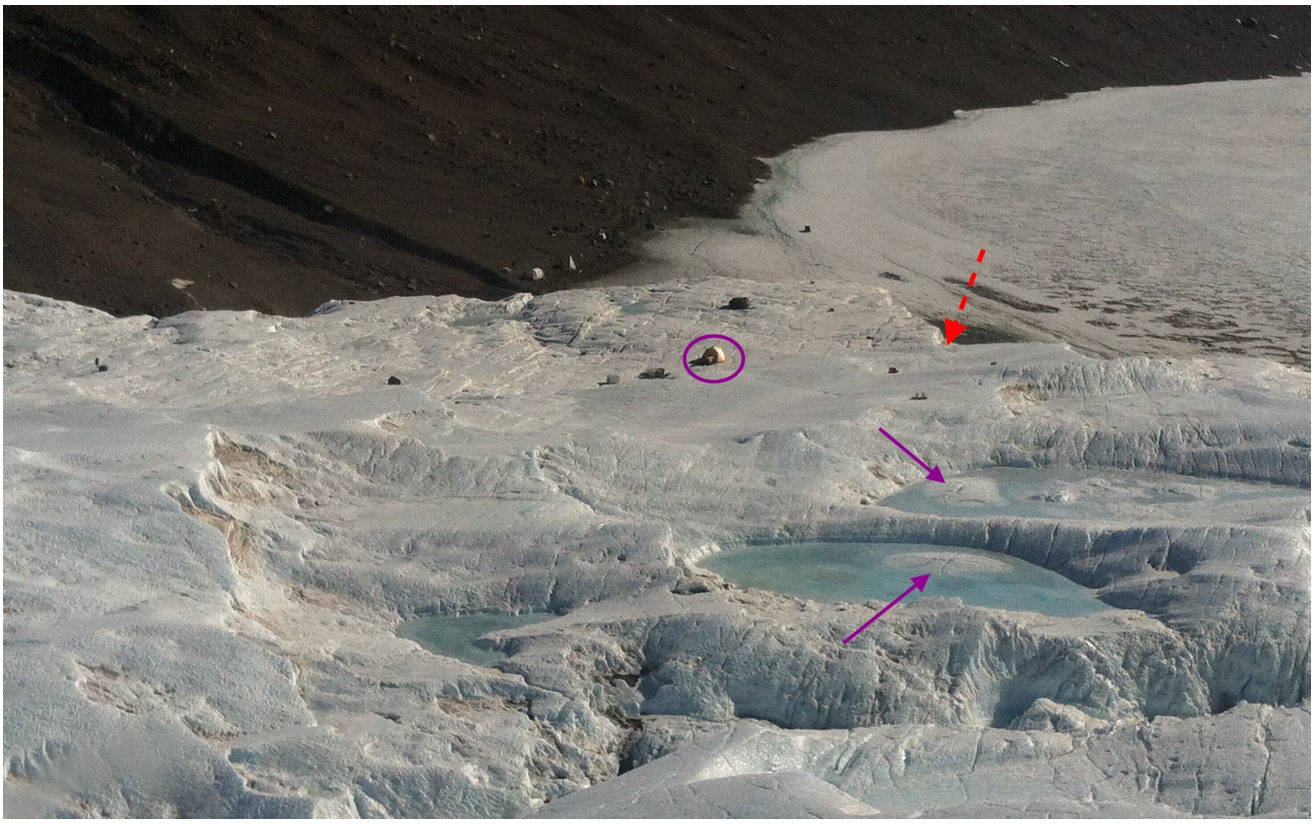

Figure S19. Ice blisters near Blood Falls. Two purple arrows mark ice blisters. The red dashed arrow points to the Blood Falls area of the terminus (out of view). For scale, a tent is circled in purple, this tent is in approximately the same location as the circled people in Figure S1. Photo: Chris Carr, photo date: 11 December 2013.

Table S1. Rayleigh detector threshold values (ρ) and sample variance ($\hat{\sigma}$) for 10–30 May 2014 under the 5x10^{-6} CFAR condition, for a radial direction with the Blood Falls back azimuth. By definition, each 30-minute window has a single threshold value. We estimate the 30-minute window sample variance as the mean of the sample variance of the 15 noise samples from that window. For each noise sample, we calculate the median of the individual sample variances, see table footnotes.

Station	Mean* ρ	Mean** $\hat{\sigma}_R^2$	Mean** $\hat{\sigma}_Z^2$
CECE	0.7049	42.98	59.00
KRIS	0.7248	123.0	658.2
JESS	0.7233	2203	1073

* $\frac{1}{m}\sum_1^m \rho_m$; where $m = 1800$, the number of 30-minute windows.
** $\frac{1}{m}\frac{1}{n}\sum_1^m\sum_1^n[\text{median}(\hat{S}^2)]_{m,n}$; m as above;
and $n = 15$, the number of noise samples.